Review | Open Access

Microstructures

Chen *et al. Microstructures* **2026**, *6*, 20260143 **DOI:**10.20517/microstructures.2026.204

Electrocatalytic CO_2 reduction to multi-carbon products with copper-based materials: from mechanistic understanding to selectivity control

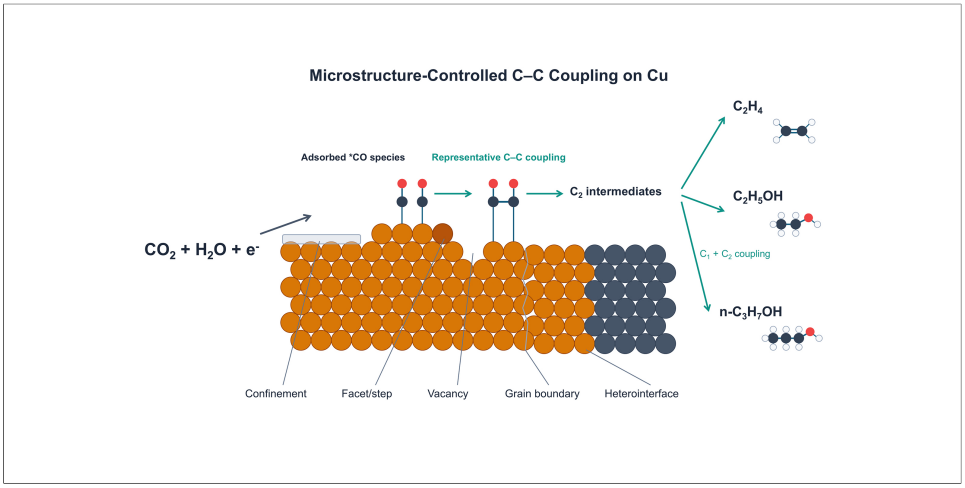
Yaoyao Chen[1,#], Zhen Wang[2,#], Yizhao Li[1]

Keywords:
CO_2 electroreduction, copper-based catalysts, multi-carbon products, C-C coupling, interfacial microenvironment, operando characterization

Citation: Chen, Y.; Wang, Z.; Li, Y. Electrocatalytic CO_2 reduction to multi-carbon products with copper-based materials: from mechanistic understanding to selectivity control. *Microstructures* **2026**, *6*, 20260143. https://dx.doi.org/10.20517/microstructures.2026.204

Received: 29 Jul 2026 **First Decision:** 26 Aug 2026 **Revised:** 26 Sep 2026 **Accepted:** 9 Oct 2026 **Published:** 17 Nov 2026

Academic Editor: Yida Deng **Copy Editor:** Fangling Lan **Production Editor:** Fangling Lan



Abstract

Coupling electrocatalytic CO_2 reduction reaction (eCO_2RR) with renewable electricity enables the synthesis of multi-carbon (C_{2+}) products—including ethylene, ethanol, and acetate—under mild conditions. Despite the ability of copper (Cu)-based catalysts to yield a diverse array of carbonaceous products, the concurrent occurrence of multi-electron transfer, C-C coupling, and the hydrogen evolution reaction makes it challenging to simultaneously achieve high activity, single-product selectivity, and long-term stability. Therefore, this review summarizes recent advances in Cu-based catalysts for the electrosynthesis of C_{2+} products based on eCO_2RR from a multi-scale perspective, followed by a critical evaluation of crystal facet engineering, defect engineering, oxidation state modulation, bimetallic synergy, and interfacial microenvironment regulation. Additionally, we highlight the application of *in situ*/operando characterization techniques and theoretical

[1]Huzhou Key Laboratory of Smart and Clean Energy, Yangtze Delta Region Institute (Huzhou), University of Electronic Science and Technology of China, Huzhou 313001, Zhejiang, China.
[2]Strait Institute of Flexible Electronics (SIFE, Future Technologies), Fujian Key Laboratory of Flexible Electronics, Key Laboratory of Optoelectronic Science and Technology for Medicine of Ministry of Education, Fujian Provincial Key Laboratory of Photonics Technology, Fujian Normal University, Fuzhou 350117, Fujian, China.
[#]Authors contributed equally.

Correspondence to: Dr. Zhen Wang, Strait Institute of Flexible Electronics (SIFE, Future Technologies), Fujian Key Laboratory of Flexible Electronics, Key Laboratory of Optoelectronic Science and Technology for Medicine of Ministry of Education, Fujian Provincial Key Laboratory of Photonics Technology, Fujian Normal University, Fuzhou 350117, Fujian, China. E-mail: qbx20220164@yjs.fjnu.edu.cn; Prof. Yizhao Li, Huzhou Key Laboratory of Smart and Clean Energy, Yangtze Delta Region Institute (Huzhou), University of Electronic Science and Technology of China, Huzhou 313001, Zhejiang, China. E-mail: yizhao@csj.uestc.edu.cn

modeling to identify reaction intermediates and track their dynamic evolution throughout the catalytic process. Finally, we discuss the challenges and prospects facing the field of eCO_2RR to C_{2+} products, and offer nuanced insights for the future design of high-efficiency Cu-based catalysts.

INTRODUCTION

Renewable electricity, particularly from wind and solar sources, is inherently intermittent; converting it into chemical energy offers a viable pathway to balance supply and demand while reducing carbon emissions from chemical manufacturing[1-4]. Electrocatalytic CO_2 reduction reaction (eCO_2RR) employs water and CO_2 as feedstocks to yield carbon monoxide, formate, methane, and a variety of hydrocarbons and oxygenates under near-ambient conditions[5-7]. Compared with two-electron C_1 products, multi-carbon (C_{2+}) products such as ethylene, ethanol, acetate, and n-propanol possess higher energy densities and are better aligned with existing market demands[2,8-11]. However, the practical value of C_{2+} products depends strongly on product identity, outlet concentration, and separation requirements. Gaseous ethylene benefits from established gas-separation technologies, whereas dilute liquid oxygenates such as ethanol and acetate require energy-intensive concentration, recovery, and electrolyte management. Moreover, synthesizing C_{2+} chemicals requires neighboring carbon intermediates to encounter one another for C-C bond formation prior to sequential proton-electron transfers, all under the practical constraints of single-pass carbon efficiency (SPCE) and cell voltage[2,10,12,13]. Thermodynamic feasibility does not guarantee kinetic accessibility; on practical electrodes, competing processes such as the hydrogen evolution reaction (HER), CO desorption, and deep reduction of C_1 intermediates coexist[14,15].

Among elemental metals, Cu is the most widely established catalyst capable of producing diverse C_{2+} products at appreciable rates and selectivities under suitable conditions[16-19]. Early comparative studies by Hori *et al.*[5,6] on product distributions over pure metal electrodes revealed that Ag and Au predominantly produce CO, Cd, In, Sn, and Pb favor formate, whereas Cu and its alloys can further produce methane and multi-carbon products. Subsequently, Kuhl *et al.*[8] systematically quantified 16 distinct eCO_2RR products on metallic Cu, revealing a potential-dependent product distribution. It does not inherently favor C_{2+} formation under all conditions; rather, the moderate *CO binding on Cu—neither readily desorbing nor over-stabilized—merely establishes the prerequisite for continued coupling[2,12,20]. Whether coupling proceeds depends on working-state *CO coverage, adjacent site geometry, local water and proton activity, and the competing HER kinetics[20-22].

Another distinctive feature of Cu is its dynamic instability under operating conditions. Nanoparticles (NPs) undergo coarsening, fragmentation, dissolution-migration-redeposition, and facet reconstruction under cathodic bias, *CO adsorption, local OH^- accumulation, and electric field effects[9,23,24]; whereas oxide-derived Cu may additionally undergo rapid reduction during the initial reaction stage[25]. These structural complexities have fueled a long-standing debate over whether high C_{2+} selectivity originates from residual Cu^+ species, Cu^+/Cu^0 adjacent sites, or low-coordination metallic Cu sites formed after reduction and reconstruction. Comparison of X-ray photoelectron spectra (XPS) or crystal phases acquired before and after reaction alone is insufficient to address this issue, as the structure may evolve through entirely distinct transient states that are inaccessible to *ex situ* characterization. A recent review[26] further categorizes Cu deactivation into atomic-scale dissolution, migration, and redeposition, along with micrometer-scale reconstruction amplified by these processes. This framework underscores that the "active structure" and the "stable structure" cannot be discussed in isolation.

Existing regulation strategies can be broadly classified into two categories. The first category pertains to modifications of the Cu sites themselves, encompassing crystal facets, particle size, defects, strain, oxidation

state, and alloying with a second metal[23-25,27-30]. The second category involves alterations to the reaction environment surrounding the sites, including molecular modifiers, confined spaces, local pH, cations, electric fields, wettability, and three-phase mass transport[10,14,31-34]. Recent reviews have compiled fairly comprehensive material taxonomies from perspectives, including catalyst architecture, surface engineering, working-state valence, facet morphology, device scaling, and ethanol-directed synthesis[1,2,13,15-19,22,35-41], yet these categories are rarely isolated in practice: For example, oxide reduction not only alters the oxidation state but also generates grain boundaries and rough surfaces; hydrophobic modification modulates water and CO_2 accessibility as well as local salt concentration; bimetallic systems may modulate adsorption via ligand or strain effects while the secondary component generates *CO *in situ* to feed Cu[20,21,33,42-45]. When Faradaic efficiency (FE) is compared solely based on material identity, such comparisons risk misattributing mass-transport effects to intrinsic activity, or conflating an overall C_{2+} enhancement with selective synthesis of a specific product. This also explains why performance metrics reported in different studies cannot be interpreted without reference to the testing conditions. H-type cells are limited by dissolved CO_2 mass transport and are therefore suited for comparing potential-dependent behavior and surface reaction mechanisms; gas-diffusion flow cells supply gaseous CO_2 directly, enabling substantially higher current densities, yet they introduce pronounced local alkalinization and carbonate formation; in membrane electrode assemblies (MEAs), the distributions of water, ions, and CO_2 differ again from those in the preceding two configurations[37,41]. The choice of reference electrode, geometric area normalization, catalyst loading, and crossover of liquid products can all alter the reported values. A rigorous review should first compare quantities of the same dimensionality within a given reactor configuration before discussing catalyst structure, rather than pooling peak FEs from disparate platforms into an unconditional performance ranking[2,13,22].

Although numerous reviews have summarized progress in Cu-based catalysts for the eCO_2RR, existing studies have largely focused on isolated material design strategies or collated performance data obtained across different electrolytic cell configurations. As a result, a unified framework integrating reaction mechanisms, working-state structures, and device-level microenvironments remains absent. In this Review, we start with an overview of CO_2 activation and *CO formation, and elucidate *CO-*CO, *CO-*CHO, and alternative C-C coupling pathways, alongside the competing HER that limits C_{2+} product formation. We then follow the causal chain of "structural variables → working-state active sites → intermediate coverage → product distribution" to conduct a critical assessment of facet engineering, defect engineering, oxidation-state regulation, bimetallic catalyst design, dynamic reconstruction regulation, and interfacial microenvironment engineering [Figure 1]. We place particular emphasis on how local pH, cations, water activity, and three-phase mass transport collectively determine the reaction pathway. Finally, to address the long-standing challenge of simultaneously achieving high C_{2+} selectivity, high operating current density, high carbon utilization, and long-term operational stability, we outline key unresolved challenges and future research directions, including dynamic active-site identification, standardized performance evaluation protocols, device upscaling, and machine-learning-assisted catalyst design.

REACTION MECHANISM OF C_{2+} FORMATION: FROM CO_2 TO C_{2+} PRODUCTS

Thermodynamically, the equilibrium potentials of most common C_{2+} products are not extremely negative, yet their formation demands surmounting kinetic barriers associated with CO_2 activation, C-C coupling, and multiple proton-electron transfers[10,13,21]. The applied overpotential serves primarily to accelerate these sluggish steps without altering the conservation of carbon, electrons, and protons[46-49]. Quantum-mechanical free-energy calculations with explicit water describe CO formation on Cu(100) through a carboxyl (*COOH) intermediate before the formation of adsorbed *CO[50]. C-C bond formation is not an isolated elementary step but rather a pathway network jointly dictated by *CO supply, surface coverage, adjacent site availability, and protonation kinetics[51,52]. Although most evidence converges on *CO as the key intermediate for C_{2+}

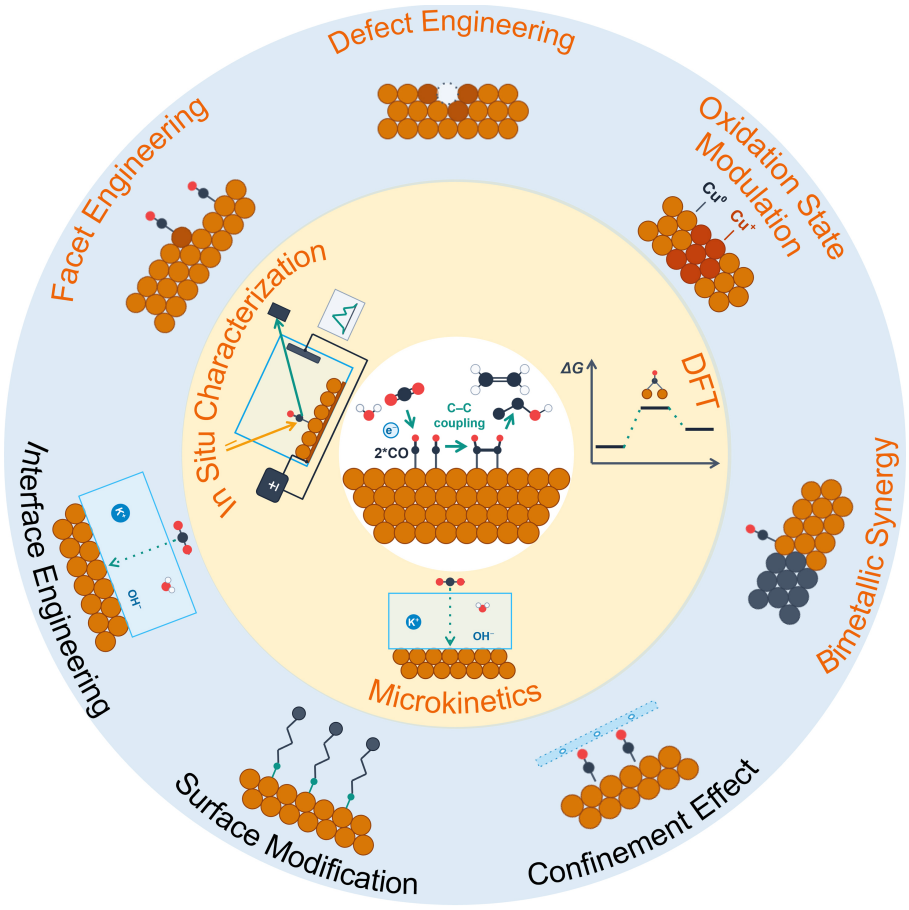


Figure 1. Strategies for designing and analyzing copper-based electrocatalysts for C_{2+} products.

formation on Cu, competing routes—including direct *CO dimerization, *CO coupling with hydrogenated intermediates, and *CO insertion—may switch as a function of potential, crystallographic facet, and local environment[53-55]. Critically, even after the first C-C bond is forged, ethylene, ethanol, and acetate continue to share common intermediates, so that elevating total C_{2+} selectivity does not necessarily translate into enhanced selectivity toward any single product. As depicted in Figure 2, the diverse pathways of the CO_2 reduction reaction give rise to a variety of intermediates, including C_1 and C_{2+}, and entail multiple electron- and proton-transfer steps.

Key intermediates

In eCO_2RR, C-C coupling requires an appropriate balance between *CO binding strength, surface coverage, and adjacent-site availability[12]. However, excessively strong *CO adsorption may over-saturate and block contiguous active sites, thereby impeding subsequent C-C coupling and proton-coupled electron-transfer steps; conversely, overly weak interaction promotes premature *CO desorption to yield C_1 products instead of further C_{2+} product formation[2,13]. Selectivity between CO_2 reduction and the HER is thus governed not merely by adsorption energy, but by applied potential, local water activity[45], site geometry, and steady-state coverage[20-22]. C-C bond formation requires at least two carbon-containing species to occupy adjacent sites in a suitable configuration. Thus, actual selectivity correlates more closely with *CO coverage, the ratio of atop- to bridge-site adsorption, surface site density, and the supply rate and residence time of *CO than with a single adsorption energy[20,21].

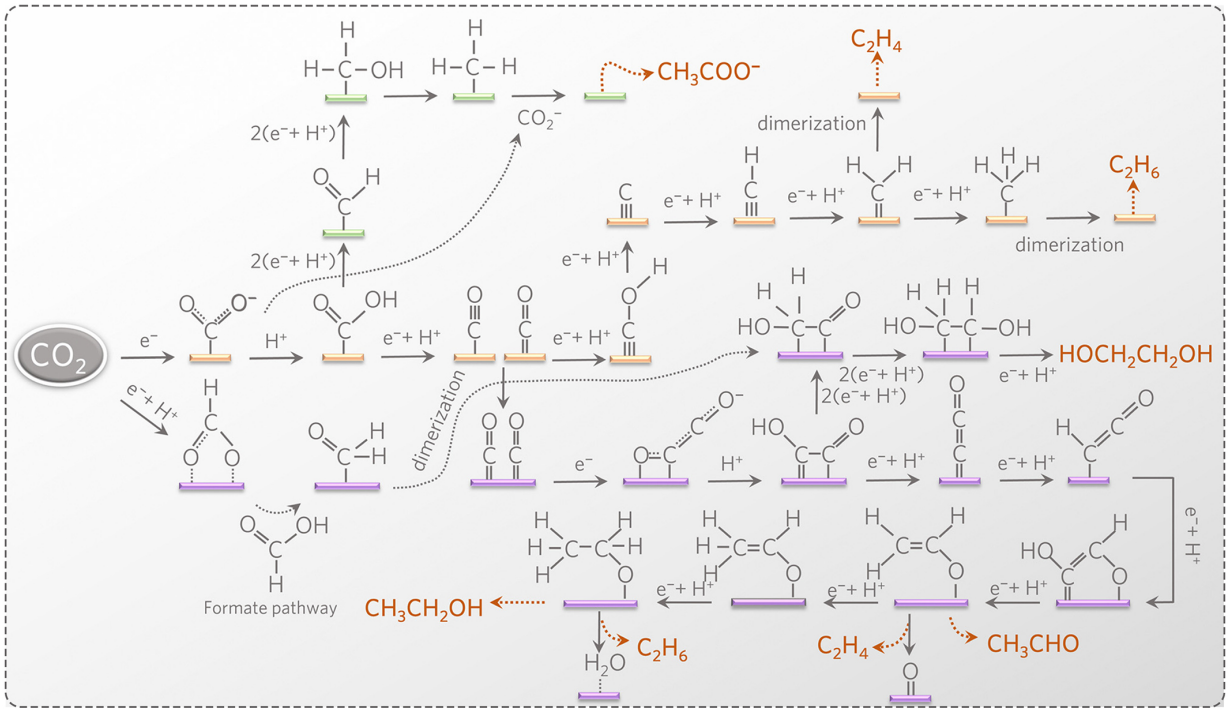


Figure 2. Overview of reaction pathways for eCO_2RR toward different C_{2+} products. Reproduced with permission[13]. Licensed under CC BY-NC 3.0.

Modulating the *CO intermediate is a key strategy for enhancing C_{2+} selectivity. At insufficient *CO coverage, the encounter probability of two surface species is too low, whereas at excessive coverage, the depletion of vacant sites impedes the participation of water and protons in subsequent steps[22]. Under elevated *CO coverage, two *CO species couple to form *OCCO, which is protonated to *OCCOH and undergoes further dehydration and hydrogenation[49,56,57]. Huang *et al.*[58] systematically examined C_2H_4 formation across Cu single crystals, confirming its correlation with *CO coverage and demonstrating that increased coverage lowers the *CO coupling barrier. *In situ* infrared and surface-enhanced Raman spectroscopies (SERS) have captured vibrational signatures consistent with hydrogenated *CO dimers, providing direct evidence for the involvement of *OCCOH in the C_2 pathway. Zhan *et al.*[20] further combined *in situ* SERS with theoretical calculations, proposing that *OC-CO(H) formed on undercoordinated Cu sites favors the ethylene route, whereas *$OCHCH_2$ stabilized on compressed or distorted Cu domains correlates with ethanol formation. This work elevates the concept of domain-dependent post-coupling branching to the realm of observable intermediates; these vibrational signatures are nonetheless influenced by local electric fields, coverage, solvent environment, and adsorption geometry, necessitating corroboration from both computed vibrational frequencies and concomitant product formation rates.

The intermediates formed after C-C bond formation govern the competition between oxygen retention and deoxygenation[59-61]. *COCOH, *COCHO, *CCO, and *CH_2CHO are commonly invoked to depict the shared network leading to ethylene, ethanol, and minor oxygenated C_2 products[28]. In general, C-O bond cleavage and dehydration favor ethylene formation, whereas stabilization of the oxygen-containing terminus and suppression of premature deoxygenation direct selectivity toward ethanol or acetate[62,63]. Zhuang *et al.*[24] constructed a Cu_2S-Cu vacancy core-shell structure that did not simply enhance all C_{2+} products but instead redirected the post-coupling branch toward multi-carbon alcohols, experimentally demonstrating that "promoting coupling" and "tuning post-coupling selectivity" are two distinct challenges. For C_{3+} products, an

existing C_2 intermediate must further couple with *CO, a step whose probability is further constrained by intermediate residence time and spatial adjacency. Consequently, beyond the pivotal intermediate *CO, the reaction pathway following *CO formation must also be rationally tuned to predict the catalytic activity and C_2 product selectivity of Cu-based catalysts.

Competing pathways in C-C coupling

C-C bond formation during eCO_2RR toward C_{2+} products has been proposed to proceed through multiple pathways, predominantly involving the coupling of *CO-derived intermediates, with their relative contributions depending on catalyst structure, electrolyte, and interfacial reaction conditions[13]. The most widely discussed routes include direct dimerization of two *CO species and asymmetric coupling between *CO and hydrogenated intermediates such as *CHO or *COH. Additional system-specific routes, including asymmetric coupling between $*CH_x$ and *CO, have also been proposed[2,12,13,24]. These proposed pathways are not necessarily mutually exclusive, and their relative contributions may vary with applied potential, *CO coverage, crystal facet, local pH, and interfacial microenvironment. Consequently, an increase in total C_{2+} selectivity neither uniquely identifies the operative coupling pathway nor demonstrates selective enhancement of a particular product branch.

In general, direct *CO dimerization is one of the most widely accepted mechanisms for C-C coupling[20,64]. Cu(100)/Cu(111) interfacial sites provide distinct ensembles that facilitate CO dimerization during CO_2 electroreduction relative to the individual low-index surfaces[65]. Based on the potential and pH dependence of single-crystal electrodes, Schouten *et al.*[12] proposed that C_1 products form via *CHO, whereas C_2 products arise from *CO dimerization and its subsequent enediol/oxametallacycle intermediates. Following protonation of *OCCO to *OCCOH, the intermediate can undergo dehydration, hydrogenation, or C-O bond cleavage, leading to ethylene, ethane, or minor oxygenated C_2 products. Nevertheless, idealized surface models do not adequately incorporate high coverage, explicit solvation, cations, and adsorption-induced reconstruction; accordingly, "Cu(100) promotes dimerization" should be regarded only as a structural trend valid under specific conditions[27,51].

The second pathway involves asymmetric coupling of *CO with hydrogenated species such as *CHO or *COH[66]. Combined theoretical and experimental evidence suggests that direct *CO dimerization may prevail at lower overpotentials and higher *CO coverage, whereas at more negative potentials, where *CHO formation accelerates, the relative contribution of the *CO-*CHO pathway increases[56,67]. In Ag single-atom alloys [Figure 3A and B], Wang *et al.*[67] showed that isolated Ag promotes water dissociation and *CHO formation, thereby enhancing *CO-*CHO asymmetric coupling and increasing the ethanol-to-ethylene ratio from 0.41 to 4.26. This result supports the interpretation that modulating the first protonation step can alter the coupling mode; although the second metal may simultaneously modify local CO supply, such that isotope-labeling and site-spacing experiments are still required to rule out alternative explanations. On histidine-modified Cu, Lim *et al.*[32] proposed coupling between histidine-bound CO and *CHO. Following *CO-*CHO coupling, the *COCHO intermediate can undergo further hydrogenation while retaining the oxygenated terminus, thereby favoring ethanol over ethylene.

As a catalyst- and condition-specific alternative to symmetric *CO dimerization, asymmetric coupling between $*CH_3$ and *CO can contribute to multi-carbon oxygenates. Isotope-labeled co-reduction experiments on Cu detected labeled acetaldehyde, ethanol, acetic acid, and acetone when $^{13}CH_3I$ and ^{12}CO were supplied as the methyl and carbonyl sources, respectively, providing experimental evidence for $*CH_3$-*CO coupling under the tested conditions[70]. In contrast, co-reduction of $^{13}CH_3I$ with $^{12}CO_2$ did not yield labeled acetate, arguing against direct coupling of $*CH_3$ with CO_2 or $*CO_2^-$ in that system. The Cu_2S-Cu vacancy core-shell catalyst directs the post-coupling branch toward higher alcohols rather than ethylene,

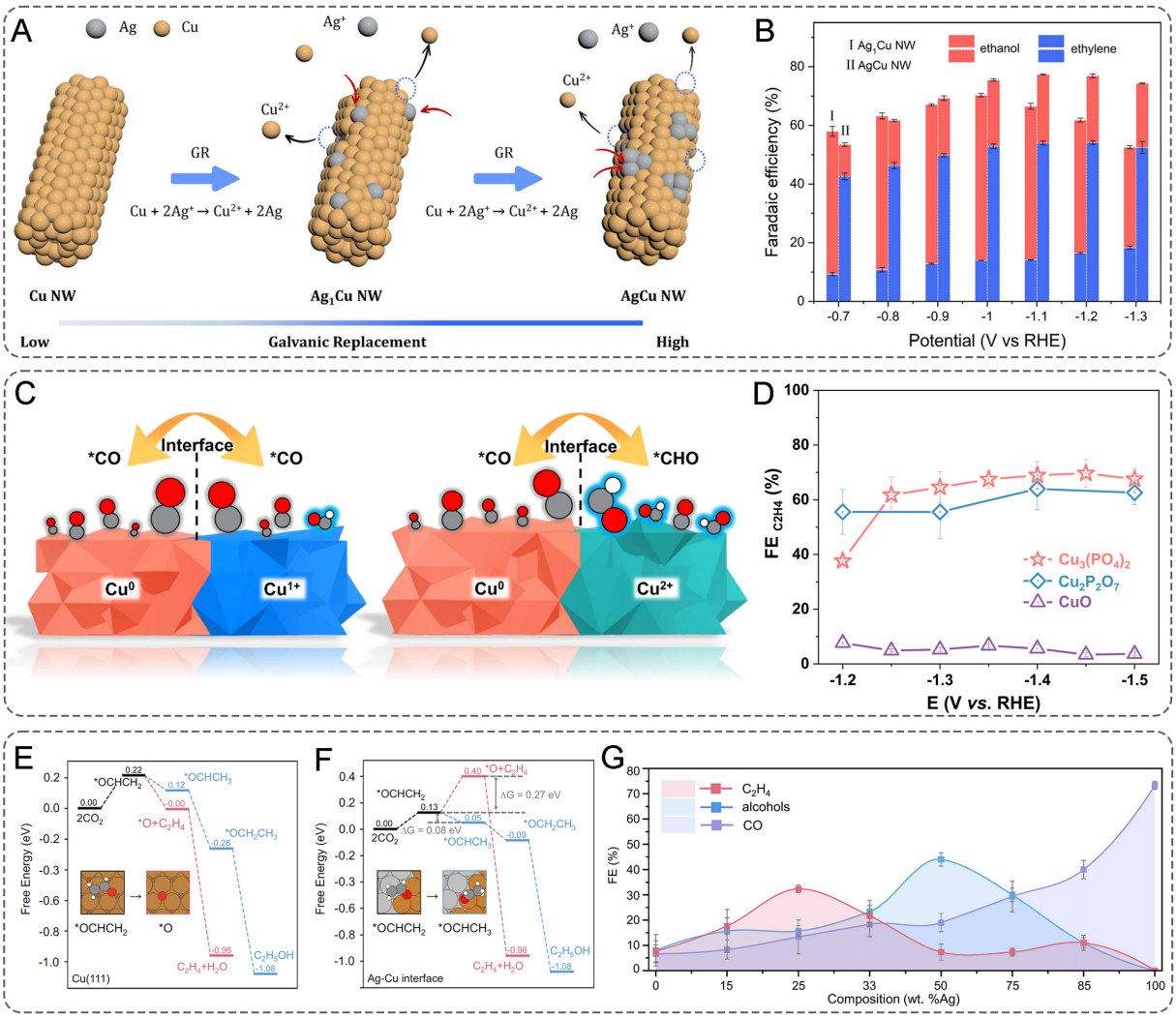


Figure 3. (A) Schematic illustration showing synthesis of Ag_1Cu NW and AgCu NW (Ag (gray) and Cu (yellow)); (B) FEs of ethanol and ethylene on Ag_1Cu NW and AgCu NW at various applied potentials. (A and B) Reproduced with permission[67]. Licensed under CC BY-NC-ND 4.0; (C) Schematic diagram of different intermediates (CO or CHO) on the Cu^0/Cu^+ and Cu^0/Cu^{2+} interfaces; (D) FEs of C_2H_4 of catalysts at different applied potentials in CO_2-saturated 0.1 M $KHCO_3$, suggesting the superior C_2H_4 selectivity for CuPO. (C and D) Reproduced with permission[68]. Licensed under CC BY 4.0; Reaction profiles for C_2H_4 and C_2H_5OH pathways on (E) Cu(111) and (F) the Ag-Cu interface; (G) The FEs of C_2H_4, alcohols and CO as a function of Ag fraction. Error bars represent the standard deviation based on three separate measurements. (E-G) Reproduced with permission[69]. Licensed under CC BY-NC-ND 4.0. NW: Nanowires; FE: Faradaic efficiency.

indicating that "promoting coupling" and "tuning post-coupling selectivity" are two separable objectives[24]. Recent studies on CO_2-to-ethanol conversion have demonstrated efficient ethanol production by suppressing deoxygenation steps[14]. This observation supports the view that competition between oxygen retention and deoxygenation of post-coupling intermediates can influence product branching. Unlike direct dimerization, asymmetric coupling does not require site-adjacency of identical species, and downstream product selectivity remains constrained by the generation of key intermediates and post-coupling branching[46].

Operando studies have identified potential-dependent surface OH/CO populations, whereas ketene-like $*CH_2CO$ intermediates have been implicated in product branching at low-coordinated Cu sites[71,72]. More broadly, these observations, together with catalyst-specific studies of atomically dispersed Cu sites under acidic conditions, indicate that interfacial species and local coordination environments can influence C_{2+} selectivity[71-73]. None of these reports, however, establishes a generally applicable formate-derived $*OCH_2$

dimerization pathway. Acetaldehyde has also been observed over Cu cluster catalysts under conventional conditions[74], illustrating that C_2 oxygenate branching may extend beyond ethanol and acetate. Selective C-O bond cleavage in $*CH_2CHO$ is an important step governing ethylene selectivity[46], while direct *OC-CHO coupling at Cu^0/Cu^{2+} interfaces has been proposed to promote C_{2+} formation [Figure 3C and D][68]. Cu-vacancy-containing heterostructures further illustrate how site heterogeneity can redirect post-coupling pathways toward oxygenated products[24].

The branch among different C_2 products is also condition-dependent. Ethylene and ethanol can share intermediates such as $*CH_2CHO$, and the relative affinity of the catalytic surface for the C- and O-termini, the availability of protons, and water activity jointly determine the subsequent hydrogenation site[13,24,45]. The Ag-Cu biphasic system provides a representative example of how interfacial composition regulates this post-coupling branch. Relative to Cu(111), the Ag-Cu interface suppresses O-C bond cleavage of $*OCHCH_2$ and favors its further hydrogenation to $*OCHCH_3$, thereby shifting selectivity from ethylene toward ethanol [Figure 3E and F][69]. Consistently, the product distribution evolves from ethylene-rich at Cu-rich compositions to alcohol-rich at an intermediate Ag fraction and finally to CO-dominated on Ag-rich surfaces [Figure 3G][69]. By contrast, acetate formation is frequently linked to the hydrolysis of ketene-like intermediates in solution or surface oxygen-retention pathways, making its selectivity particularly sensitive to local pH and interfacial residence time[14,68]. The formation of C_{3+} products requires an additional coupling step beyond the initial C-C bond formation. For n-propanol, undercoordinated Cu sites have been demonstrated to strengthen the adsorption of key surface C_2 intermediates, thereby facilitating the subsequent C-C coupling steps required for C_3 synthesis. Accordingly, C_3 selectivity depends on generating and stabilizing the C_2 intermediate sufficiently on the catalyst surface[75]. Extending the pore residence time may favor the second coupling, yet it may also promote the re-adsorption of intermediates such as acetaldehyde[76]. Critically, while initial C-C coupling establishes the overall capacity for C_{2+} formation, subsequent intermediate branching determines product-specific selectivity—governing whether the reaction channels toward deoxygenated gaseous ethylene or oxygen-retaining liquid products such as ethanol and acetate.

HER competition

HER is an inevitable competing pathway in aqueous eCO_2RR, as both reactions compete for electrons, interfacial water, and surface adsorption sites[34,73,77]. In the low-overpotential regime, sluggish CO_2 activation and insufficient *CO coverage cause HER to dominate the current partition; as the potential shifts more negative, *CO accumulation and the probability of C-C coupling increase, thereby enhancing C_{2+} selectivity. However, further polarization accelerates water reduction and deep hydrogenation of *CO, causing H_2 and CH_4 selectivities to rise. This non-monotonic behavior implies that C_{2+} selectivity typically reaches a peak within a specific potential window rather than increasing continuously with cathodic bias[2,8].

The competition is governed not only by potential but also by the local microenvironment. At high current densities, proton consumption at the interface is accompanied by OH^- generation, causing the local pH to rise to alkaline levels[78,79]. This shift can suppress the HER that directly involves protons and provide more favorable *CO coverage for C-C coupling. However, OH^- simultaneously captures CO_2 to form carbonates, reducing the SPCE[80]. SPCE quantifies the fraction of inlet carbon incorporated into specified products during a single pass, a feature that is not captured by FE alone[81,82]. The SPCE toward C_{2+} products is defined as the fraction of carbon in the inlet CO_2 stream that is incorporated into C_{2+} products during a single pass. Based on carbon balance and Faraday's law, it can be calculated as follows:

$$SPCE = \frac{\left\{\sum_i \left[\frac{c_i |j_i| A \times 60}{z_i F}\right]\right\}}{\frac{Q_{CO_{2,in}}}{V_m}} \times 100\% \quad (1)$$

where j_i is the partial current density of product i in A cm^{-2}, A is the geometric electrode area in cm^2, and $|j_i|A$ is the corresponding partial current in A; z_i is the number of electrons transferred per molecule of product i; c_i is the number of carbon atoms in product i; F is Faraday's constant (96,485 C mol^{-1}); $Q_{CO_2,in}$ is the inlet CO_2 volumetric flow rate in L min^{-1}; and V_m is the molar gas volume evaluated at the temperature and pressure used for flow calibration. The factor of 60 converts the electrochemical product formation rate from mol s^{-1} to mol min^{-1}, allowing it to be compared with $Q_{CO_2,in}/V_m$ in mol min^{-1}. This formulation generalizes the product-specific Faradaic-law SPCE expression established by Chen *et al.*[83] into a carbon-balanced multi-product form across all C_{2+} species. Experimentally, high SPCE values in acidic media have been demonstrated by Zhu *et al.*[84], who reported an empirical SPCE of 51.8% for C_{2+} products on a hollow-fiber Cu penetration electrode. However, da Cunha and Resasco[85] showed that maximizing single-pass conversion does not necessarily yield concentrated product streams or indicate practical electrolyzer readiness; they therefore recommended reporting outlet product concentrations rather than treating single-pass conversion alone as an overall performance indicator.

Water-activity experiments further demonstrate that proton supply is not "the less, the better": When the water activity is decreased from 0.97 to 0.47, the C_{2+}/C_1 ratio can be tuned between approximately 1 and 20, yielding a C_{2+} FE of ~73% and a C_{2+} partial current density of ~-110 mA cm^{-2} at a water activity of 0.66[45]. This indicates a narrow window among suppressing HER, sustaining C-C coupling, and completing post-coupling hydrogenation, such that merely reducing water content does not guarantee an increase in the target product.

To resolve reporting ambiguities across different electrolysis frameworks, key operational carbon and energy metrics are defined as follows: (1) single-pass CO_2 consumption: $X_{CO_2,SP} = \left[\frac{\dot{n}_{CO_2,in} - \dot{n}_{CO_2,out}}{\dot{n}_{CO_2\,in}}\right] \times 100\%$, which denotes the fraction of CO_2 removed from the feed stream during a single pass[86]; because of carbonate formation, crossover, or incomplete carbon accounting, it cannot be equated directly to target-product yield[85]. (2) Carbon efficiency (CE): the fraction of converted carbon recovered in quantified carbonaceous products, which is meaningful only when a complete carbon balance is closed across gas, liquid, and transmembrane crossover streams. (3) Target-product carbon utilization ($U_{C,target}$): the fraction of total inlet carbon converted into the target multi-carbon product, whose value strictly depends on the defined system boundaries (diverging between once-through pure CO_2 feed streams and systems involving recycle loops or carbonate capture media). (4) Full-cell energy efficiency: Operating strictly with the oxygen evolution reaction (OER) as the anodic counter-reaction, the product-specific full-cell energy efficiency is defined as[83]:

$$\eta_{EE,i} = \frac{FE_i\left(1.23V - E_i^0\right)}{|V_{cell}|} \times 100\% \quad (2)$$

where 1.23 V is the thermodynamic equilibrium potential for the OER *vs*. the reversible hydrogen electrode (RHE); E_i^0 is the standard thermodynamic equilibrium potential for the formation of eCO_2RR product i *vs*. RHE; FE_i must be substituted as a dimensionless decimal fraction between 0 and 1; and V_{cell} is the actual measured full-cell operating voltage absolute value, containing all real cell losses (including cathodic and anodic overpotentials, membrane/electrolyte Ohmic resistances, and transport polarizations), and cannot be replaced by an iR-corrected cathode potential. As a practical device-level example, Chen *et al.*[87] reported stable operation for over 300 h at 10 A with a measured full-cell voltage of 4.2-5.0 V without iR compensation. This study is cited here as an empirical high-current device example rather than as the derivation source of Equation (2).

STRATEGIES FOR CATALYST STRUCTURAL ENGINEERING

The structure and composition of a catalyst play a decisive role in substrate activation and reduction processes, thereby profoundly influencing the selectivity of the final products[59-61,88-90]. Structural regulation aims to establish a sustainable "site-intermediate-microenvironment" ensemble that persists under the operating potential. Crystal facets, defects, oxidation states, and bimetallic components primarily modulate the geometric and electronic structures of active sites; confinement effects, molecular modifiers, and the electrode-electrolyte interface directly alter reactant supply, local electric fields, and proton transfer[91-93]. It should be noted that there may be some overlap of different categories of methods and very often more than one strategy is needed to design and synthesize a catalyst with a desirable structure.

Facet engineering

Facet engineering primarily alters the arrangement of adjacent Cu atoms and the configuration of adsorption sites, with Cu crystal facets exhibiting clear structure sensitivity toward C_1/C_2 products[27,51,65]. Single-crystal experiments and theoretical studies by Koper *et al.* revealed that Cu(100) more readily accommodates adjacent *CO to form *OCCO, leading to ethylene production, whereas Cu(111) tends to favor methane or partially oxygenated products[12,20,48,89,90,94]. Step sites and heterogeneous facet boundaries can also stabilize asymmetric intermediates such as *CHO, thereby shifting the distribution between ethylene and oxygenated C_{2+} products[91]. The geometric basis lies in the differing adsorption sites for *CO, the distances between neighboring Cu atoms, and the constraints imposed on *OCCO configurations across different facets[95]. However, elevated *CO coverage can alter the ratio of atop to bridge-bonded *CO, and adsorption-induced reconstruction may transform the initial facets into steps, island-like, or mixed orientation structures[96].

Nanocubes (NCs) are commonly employed to enrich (100) facets, yet particle size and the proportion of edge/corner sites vary concurrently with the exposed facet. Loiudice *et al.*[23] compared Cu NCs of 24, 44, and 63 nm and observed a non-monotonic size effect, with the 44 nm sample exhibiting the highest CO_2 reduction FE of 80% and an ethylene FE of 41% [Figure 4A-G]. On the other hand, Reske *et al.*[9] found that smaller Cu particles tend to promote H_2 and CO generation. These results indicate that excessively large particles reduce the number of exposed active sites per unit mass, while excessively small particles increase the fraction of undercoordinated edge/corner sites and disrupt contiguous Cu site ensembles. Therefore, C-C coupling requires an optimal balance between continuous terrace sites and low-coordination boundary sites, rather than simply pursuing the smallest possible particle size.

The actual performance differences attributable to the crystal planes can only hold true when the working state structure and mass transfer conditions are comparable. Cu cubes can undergo edge disintegration, pitting, coarsening, and grain rotation during reaction; consequently, the pre-reaction proportion of (100) facets cannot represent the steady-state surface[25,62,63,97-102]. Yao *et al.*[51] directly exploited CO/OH^- co-adsorption to induce working-state faceting and form a Cu(100)-rich surface. In addition, Zhao and Ren[27] compared the facet response of different derived Cu catalysts under unified mass transport conditions. These studies demonstrate that facet-related conclusions must be evaluated in conjunction with potential, coverage, and reaction time. More specifically, the Cu(100)/Cu(111) interface constructed by Wu *et al.*[65] achieved a C_{2+} FE of 74.9% ± 1.7% and a current density of 300 mA cm^{-2} in 1 M $KHCO_3$, with continuous operation for 50 h [Figure 4H and I]; this result supports heterogeneous facet boundaries as candidate coupling sites, yet cannot exclude contributions from local roughness and mass transport. More reliable attribution requires identical electrolyte, potential, and time scales, along with simultaneous correlation of crystal structure changes with partial product rates. Consequently, when translating single-crystal trends to powder electrodes, the exposed-facet ratio, electrochemical active surface area (ECSA), and reconstruction pathways must be quantified; only when these variables are comparable does the comparison of "intrinsic facet selectivity" carry explanatory power[91].

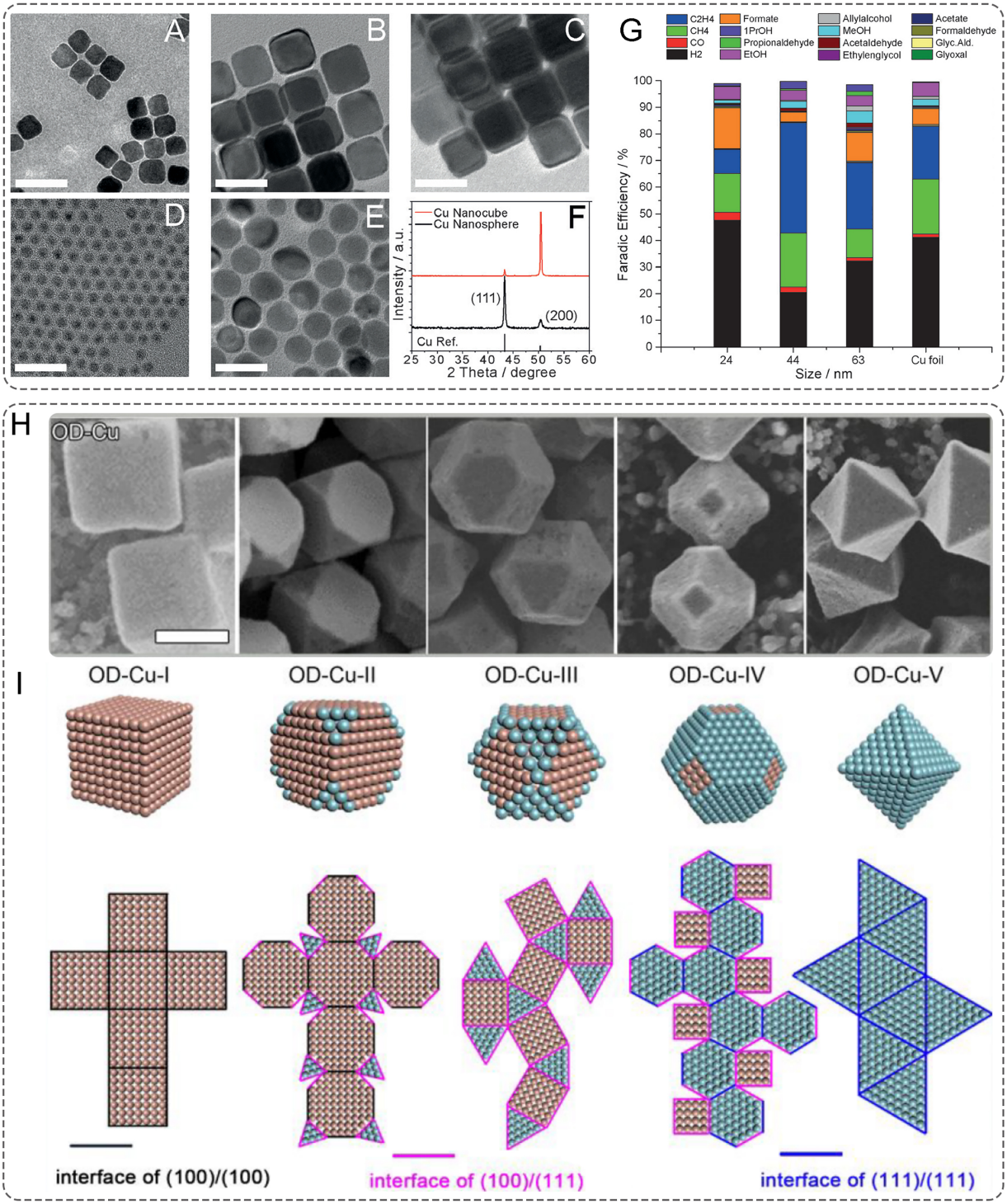


Figure 4. (A-C) TEM images of Cu cubes with an average edge length of 24, 44, 63 nm, respectively; (D and E) TEM images of Cu spheres with an average diameter of 7.5 and 27 nm, respectively. Scale bar 50 nm; (F) Typical XRD patterns of the Cu spheres (black line) and Cu cubes (red line); (G) Bar graph reporting the FEs for each product in the different sizes of Cu cubes and in the Cu foil at -1.1 V *vs*. RHE. (A-G) Reproduced with permission[23]. Copyright 2016, Wiley-VCH; (H) SEM images and (I) corresponding structure of OD-Cu derived from Cu_2O crystals. Scale bar, 400 nm. (H and I) Reproduced with permission[65]. Copyright 2022, American Chemical Society. TEM: Transmission electron microscopy; FEs: Faradaic efficiencies; XRD: X-ray diffraction; SEM: Scanning electron microscopy.

Defect engineering

The core function of defect engineering is to establish low-coordination sites and asymmetric adjacency relations on the Cu surface that are absent from conventional low-index facets[31,103]. Grain boundaries, vacancies, and strained sites can all enhance *CO coverage and create asymmetric coupling sites, but such

defects simultaneously strengthen *H adsorption, disrupt contiguous Cu site ensembles, and accelerate dissolution and reconstruction[104-113]. Fang *et al.*[107] prepared Cu_2O catalysts with varying degrees of roughness by tuning the dosage of surfactant and structure-directing agents; the catalyst with the optimal roughness achieved a C_{2+} FE of 84.2%, an ethylene selectivity of 56.3%, and a C_{2+} partial current density of 416.4 mA cm^{-2} at -1.4 V *vs.* RHE, significantly outperforming the rougher counterparts. This finding suggests that defect identity, rather than roughness alone, contributes substantially to the observed performance differences.

A complementary example is provided by hydrothermal synthesis of CuO nanosheets followed by electrochemical reduction, which produces defect-rich porous Cu nanosheets (pCu NS) [Figure 5A] that expose prominent Cu(200) lattice fringes with 0.18 nm spacing corresponding to preferentially exposed Cu(100) facets alongside abundant surface defect sites [Figure 5B][114]. When evaluated in an acidic membrane electrode assembly (0.05 M H_2SO_4 + 0.4 M K_2SO_4), pCu NS achieved a C_{2+} FE of 75.01% at 300 mA cm^{-2} and approximately 3.84 V full-cell voltage. In separate single-pass conversion tests under low gas flow rate, the catalyst delivered an overall CO_2 single-pass conversion efficiency of 74.38% and a C_{2+} single-pass conversion efficiency of 45.5% at 3 sccm and 200 mA cm^{-2}. Crucially, this performance is not governed solely by atomic defect sites, but arises from the synergistic coupling between defect-promoted *CO coverage, facet-directed coupling energetics, and the porous nanosheet architecture that optimizes local reactant transport under acidic bias.

Cu vacancies modulate product branching beyond merely promoting C-C coupling[117]. Zhuang *et al.*[24] reported a Cu_2S-Cu vacancy core-shell catalyst that, under flow-cell conditions, delivered a C_{2+} alcohol partial current density of 126 ± 5 mA cm^{-2} and a FE of 32% ± 1%, both approximately twice those of the vacancy-free Cu_2S and pure Cu controls, and enhanced the alcohol-to-olefin ratio more than sixfold. By comparison, Ni atomic cluster decoration of defect-rich Cu primarily improved *CO supply: The C_{2+} FE increased to 44% in H-type cells and further to 62% in flow cells[118]. Cu vacancies modulate the oxygen-retention versus deoxygenation branching, whereas Ni clusters reinforce upstream *CO generation, demonstrating that "defect-promoted C_{2+} production" can correspond to entirely different rate-limiting steps.

Vacancies formed during the reaction can also enable high-current performance. $Cu_{1.8}Se$ reconstructed at -450 mA cm^{-2}, accompanied by Se leaching and Cu vacancy formation, achieving a C_{2+} FE of 64.26% ± 0.8%, surpassing those of CuSe (40.6%) and Cu_2Se (42.1%), and sustaining operation for 38 h at the same current density[103]. Oxide-derived porous Cu raised the C_{2+} FE from less than 18.2% for polished Cu to 62.7%, with the ethylene partial current increasing from 0.1 to 35.7 mA cm^{-2}[106]. However, both studies involved concurrent changes in porosity, valence state, and local mass transport, preventing exclusive attribution of performance gains to individual vacancies or grain boundaries.

Beyond inorganic lattices, molecular coordination vacancies provide an alternative route to modulate interfacial reactivity. Defect-rich Cu-1H-1,2,3-triazole (D-Cu-triazole) synthesized with ligand-vacancy defects and coordinatively unsaturated Cu sites exhibits open metal sites that alter the local coordination environment compared to pristine Cu-triazole [Figure 5C and D][115]. During CO_2 electroreduction in 1.0 M KOH at -200 mA cm^{-2}, D-Cu-triazole achieved approximately 78.4% C_{2+} FE, markedly suppressing C_1 and H_2 generation. Importantly, post-electrolysis X-ray diffraction (XRD), XPS, and transmission electron microscopy (TEM) demonstrate that D-Cu-triazole operates as a dynamic precatalyst that undergoes reductive reconstruction under cathodic potential, suggesting that the catalytically relevant working state is associated with nitrogen-containing ligand-functionalized Cu nanoclusters rather than the intact initial framework.

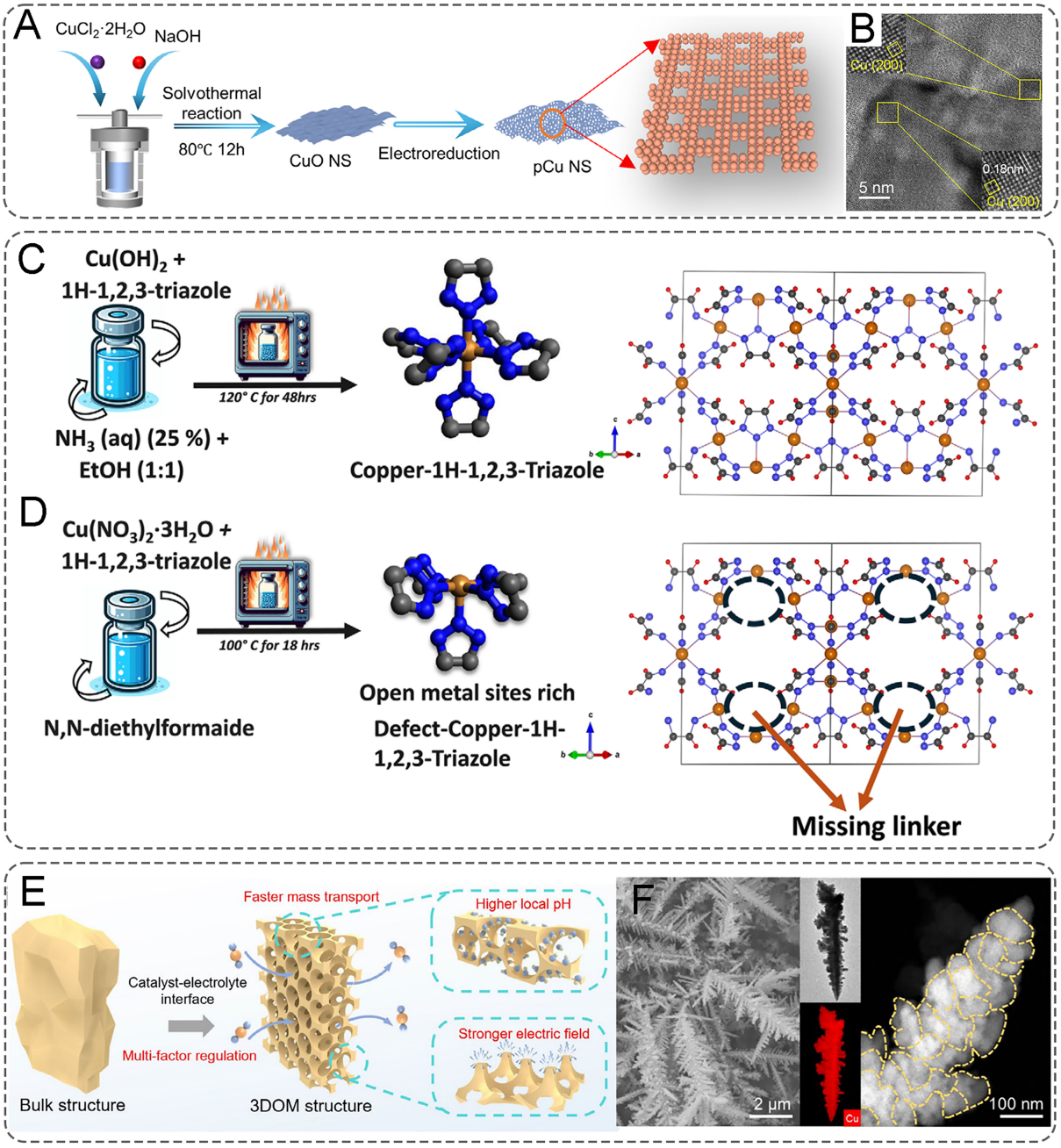


Figure 5. (A) Schematic illustration of the preparation procedure of pCu NS; (B) HRTEM image of pCu NS. (A and B) Reproduced with permission[114]. Licensed under CC BY 4.0; Synthesis scheme for (C) Cu-1H-1,2,3-triazole (Cu-triazole) and (D) defect-Cu-1H-1,2,3-triazole (D-Cu-triazole) with their corresponding crystal structure. (C and D) Reproduced with permission[115]. licensed under CC BY 4.0; (E) Schematic illustration on multi-factor interfacial regulation with 3DOM structure, giving faster mass transport, higher local pH, and stronger electric field at the catalyst-electrolyte interface; (F) SEM, TEM, STEM images, and EDS mapping of dendritic Cu^0 in 3DOM-La_2CuO_4-P. (E and F) Reproduced with permission[116]. Copyright 2026, Wiley-VCH. NS: nanosheet; HRTEM: High-Resolution Transmission Electron Microscopy; SEM: Scanning electron microscopy; TEM: Transmission electron microscopy; STEM: Scanning Transmission Electron Microscope; EDS: Energy-dispersive X-ray spectroscopy.

Furthermore, defect density and active phase stability can be directed by the structural microenvironment. Constructing a three-dimensionally ordered macroporous (3DOM) architecture from layered perovskite La_2CuO_4 establishes a multi-factor interfacial microenvironment that concurrently accelerates mass transport, elevates local pH, and intensifies the surface electric field [Figure 5E][116]. This tailored local environment drives an accelerated and complete reconstruction of the initial 3DOM-La_2CuO_4-P precatalyst

into dendritic metallic Cu rich in strained grain boundaries, as characterized by scanning electron microscopy, TEM, energy-dispersive X-ray spectroscopy elemental mapping, and high-angle annular dark-field scanning transmission electron microscopy (STEM) [Figure 5F]. Theoretical and electrochemical analyses indicate that undercoordinated and compressively strained Cu atoms at grain boundaries facilitate *COH formation and stabilize *OCCOH intermediates while suppressing the competing HER. Consequently, the catalyst delivers a C_{2+} partial current density of 585 mA cm^{-2} in a flow cell, and sustains continuous operation for approximately 200 h at 600 mA cm^{-2} in a membrane electrode assembly.

In addition, strain and grain boundaries determine whether defects can persist over the long term. Derived Cu develops local strain during reduction, yet this strain can be relieved through coarsening[28,88]; nano-focused X-ray studies on the Cu-Ag system revealed that Ag-induced strain and corrosion-resistant stability evolve concurrently[117]. Consequently, adsorption energy changes arising from strain need to be verified under identical size and defect density conditions. Strain is frequently coupled with defects. Compressive or tensile strain can shift the electronic states of Cu and alter the adsorption of *CO, *H, and oxygenated intermediates, but strain distribution in NPs is inherently non-uniform and can also be relieved through reconstruction during the reaction. Attributing performance entirely to the average lattice constant risks overlooking local boundaries that are mechanistically relevant[1,2,103].

Oxidation state modulation: dynamic equilibrium at the Cu^+/Cu^0 interface

Beyond facet and defect engineering, oxide-derived Cu catalysts significantly improve eCO_2RR performance by creating mixed valence states and inducing synergistic interactions between Cu^0 and Cu^+ species[119-125]. Some density functional theory (DFT) models suggest that Cu^0 facilitates electron transfer while Cu^+ enhances *CO adsorption and stabilizes *OCCO, thereby lowering the coupling free energy; various oxide-derived Cu catalysts have also shown residual Cu^+ in *ex situ* characterization correlated with elevated C_{2+} selectivity[68,126-134]. de Ruiter *et al.*[25] observed that Cu_2O was fully converted to metallic Cu within 40 s after the onset of cathodic bias; subsequently, the surface continued to coarsen, accompanied by a decline in C_2 hydrocarbon selectivity over approximately 30 min [Figure 6A-D]. This result indicates that the higher initial C_{2+} performance may originate from oxide-inherited porosity and low-coordinated metallic Cu, and does not necessarily imply the presence of steady-state bulk Cu^+. In parallel, the soluble Cu^+ carbonyl species detected by Vavra *et al.*[135] were identified as transient intermediates involved in subsequent dissolution, migration, and redeposition processes. Thus, the initial oxidation state, reconstruction transients, and steady-state surface species must be distinguished from one another.

In systems capable of maintaining mixed valence states, Cu^+/Cu^0 adjacency sites can be correlated with significant performance enhancements[137]. He *et al.*[96] demonstrated that abundant Cu_2O-Cu^0 interfaces in a well-designed nanocomposite electrocatalyst are critical for significantly promoting C_{2+} production within a MEA, achieving a current density of 1.0 A cm^{-2}, a C_{2+} FE of 80%, and a single-pass C_{2+} yield of 19%, whereas the pure Cu^0 counterpart showed virtually no C_{2+} enhancement [Figure 6E]. Wu *et al.*[130] used aryl diazonium salt functionalization to tune the Cu valence to approximately $Cu^{0.26+}$, achieving an ethylene FE and partial current density of 83% ± 2% and 212 mA cm^{-2}, respectively; after perfluorinated sulfonic acid ionomer addition, the functionalized Cu exhibited an ethylene FE and partial current density of 89% ± 3% and 536 mA cm^{-2}, *vs.* 48% ± 4% and 269 mA cm^{-2} for unfunctionalized Cu with the same ionomer. Cao *et al.*[138] constructed a $Cu^0/Cu^+/Cu^0$ interface *in situ* via comproportionation, achieving a C_2+ FE of 92.3% and a C_2+ partial current density of 276.9 mA cm^{-2} in a flow cell, and sustained over 90% C_2+ FE for more than 50 h in an MEA. Recently, Cui *et al.*[136] demonstrated that strong additive-oxide interactions can regulate the dynamic reconstruction of metastable Cu oxidation states under strongly acidic conditions. Coordination between the S=O group of dimethyl sulfoxide and surface Cu sites suppressed the complete reduction of Cu_2O, enabling controlled *in situ* reconstruction into a co-lattice OD-Cu/Cu_2O heterostructure. The

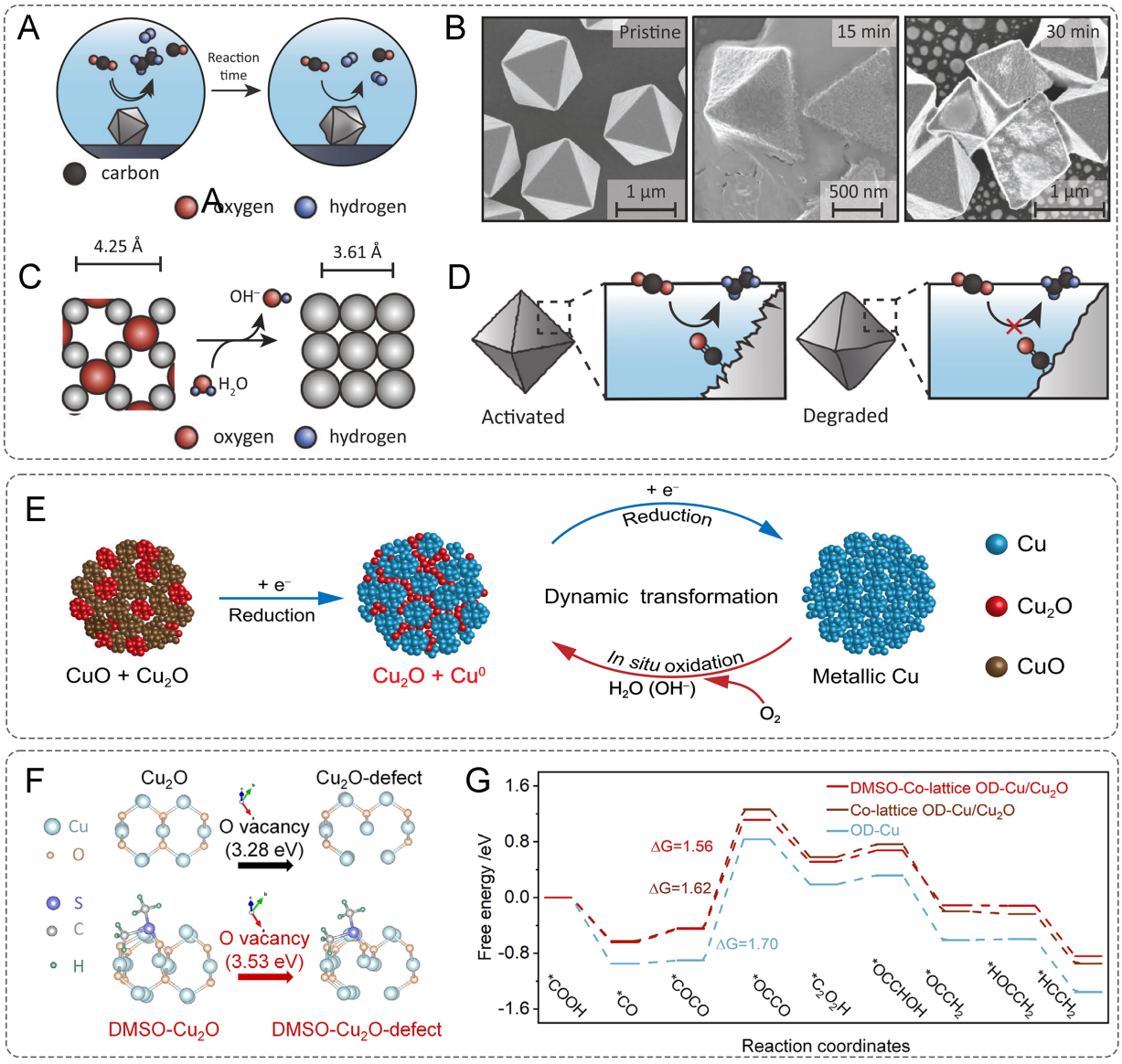


Figure 6. (A) Main products formed during electrochemical CO_2 reduction over octahedral Cu_2O electrocatalyst particles at early stages of cathodic bias (left) and after prolonged operation up to 30 min (right); (B) Representative *ex situ* SEM images of pristine Cu_2O, and electrolysis of Cu after 15 and 30 min (from left to right) at -1.0 V *vs.* RHE; (C) The shrinkage effect of electrochemical reduction on the unit cell of Cu_2O and Cu; (D) Structural changes observed with *in situ* X-ray scattering. (A-D) Reproduced with permission[25]. Licensed under CC BY-NC-ND 4.0; (E) Dynamic reduction and re-oxidation mechanism of Cu for the Cu_2O-Cu^0 catalyst during eCO_2RR. (E) Reproduced with permission[96]. Licensed under CC BY-NC-ND 4.0; (F) Oxygen vacancy formation energy of Cu_2O and DMSO-Cu_2O; (G) Gibbs free energy diagrams of CO_2RR pathways on different catalysts. (F and G) Reproduced with permission[136]. Copyright 2026, Wiley-VCH. SEM: Scanning electron microscopy; eCO_2RR: Electrocatalytic CO_2 reduction reaction; DMSO: dimethyl sulfoxide.

resulting catalyst exhibited a C_2H_4 FE of 67.5% and an H_2 FE of 16.8% at -1.5 V *vs.* RHE [Figure 6F and G]. These results support the design value of interfacial valence states, though the functional layers, local alkalinity, and mass transport are simultaneously modified.

In summary, the practical objective of oxidation state modulation should not be framed as "the more Cu^+, the better". Excessive Cu^+ may compromise electrical conductivity or impede further hydrogenation and coupling of *CO, and pure Cu^+ models have also been found inferior to mixed-valence interfaces in certain computational studies. Rigorous attribution requires experiments that probe different valence responses under comparable roughness and mass transport conditions, with transient products measured at each pulse

stage. Otherwise, all performance improvements of oxide-derived Cu should not be uniformly attributed to Cu^{+}/Cu^{0} synergy[95,135].

Bimetallic synergy

Bimetallic regulation is commonly employed to alter the activity and selectivity of eCO_2RR. The apparent synergy should not be assigned to a single universal origin. Depending on the spatial arrangement, surface composition, and working-state reconstruction, three non-mutually exclusive contributions may operate: (i) tandem CO supply, in which a CO-selective secondary component increases the local *CO availability at nearby Cu sites; (ii) electronic or strain effects, which modify the adsorption and hydrogenation energetics of key intermediates; and (iii) geometric ensemble or site-dilution effects, which alter the number and continuity of adjacent Cu sites required for C-C coupling and competing hydrogenation reactions[139-146]. Ma *et al.*[29] reported Ag_{65}-Cu_{35} with Janus {100} facets that achieved a C_{2+} FE of 67% at -1.2 V, surpassing both Cu NCs (52%) and a physical mixture of Ag and Cu (22%) [Figure 7A and B]. The potential window for ethylene FE exceeding 50% shifted to less negative potentials by approximately 400 mV relative to pure Cu, with a maximum C_{2+} FE of 72%. Cai *et al.*[30] constructed a hierarchical Ag-Cu interface that further achieved a C_{2+} FE of 80.2% and an ethanol FE of 52.6% at a total current density of approximately 320 mA cm^{-2}, demonstrating remarkable stability over 60 h. Together, these results indicate that intimate interfacial contact ensuring short *CO migration distances and contiguous Cu sites outperforms simple physical mixing of the two metals[147,148].

The atomic-scale dispersion state of Ag can steer selectivity toward different products. Wang *et al.*[67] compared Ag NP-decorated Cu (nanoparticulate Ag) with Ag single-atom alloys (atomically dispersed Ag): Nanoparticulate Ag predominantly produced ethylene, with a FE of 54.9% and a partial current density of 156.0 mA cm^{-2}; atomically dispersed Ag redirected the product toward ethanol via water dissociation and a *CHO-related pathway, achieving a FE of 56.3% and a partial current density of 172.8 mA cm^{-2}. This indicates that the secondary metal not only alters the overall C_{2+} selectivity but also modulates the initial coupling configuration and post-coupling hydrogenation through its spatial distribution.

Bimetallic composition and reconstruction also exert a considerable influence on performance. Gao *et al.*[69] designed a well-defined Ag-Cu biphasic heterostructure to tune product selectivity via interfacial structure regulation: The Cu-rich interface ($Ag_{0.25}$-$Cu_{0.75}$) favored ethylene production; as the Ag atomic fraction increased ($Ag_{0.5}$-$Cu_{0.5}$), the major product gradually shifted toward alcohols, and ultimately yielded CO when Ag dominated the surface [Figure 7C and D]. Extended operando studies showed that in Cu-Zn systems, the ethanol-to-ethylene FE ratio increased from 1.25 to 3.54 as the Zn content rose from 9 to 28 at.%, while the CO FE concomitantly increased sharply once Zn exceeded 9 at.%[76]. These results suggest that the optimal composition results from a trade-off among CO supply, dilution of Cu sites, and working-state phase distribution.

Core-shell thickness serves as a tunable parameter to investigate the cascade from *CO generation to C-C coupling[112]. In Ag@C@Cu[149] tested at 400 mA cm^{-2}, as the Cu shell became thinner, ethanol production first increased before shifting toward CO; at the optimal Ag/Cu mass ratio of 0.1, the ethanol FE reached 31.5% and a partial current density of 126 mA cm^{-2}. In an electrodeposited 3Cu:1Ag system[150], the addition of Ag raised the ethylene FE from approximately 7.9% for pure Cu to approximately 18%, yet the intrinsic partial current density did not increase proportionally, indicating that HER suppression and surface area changes also contributed to the FE improvement. Therefore, assessments of sequential CO conversion should simultaneously report CO utilization and product-specific partial current densities.

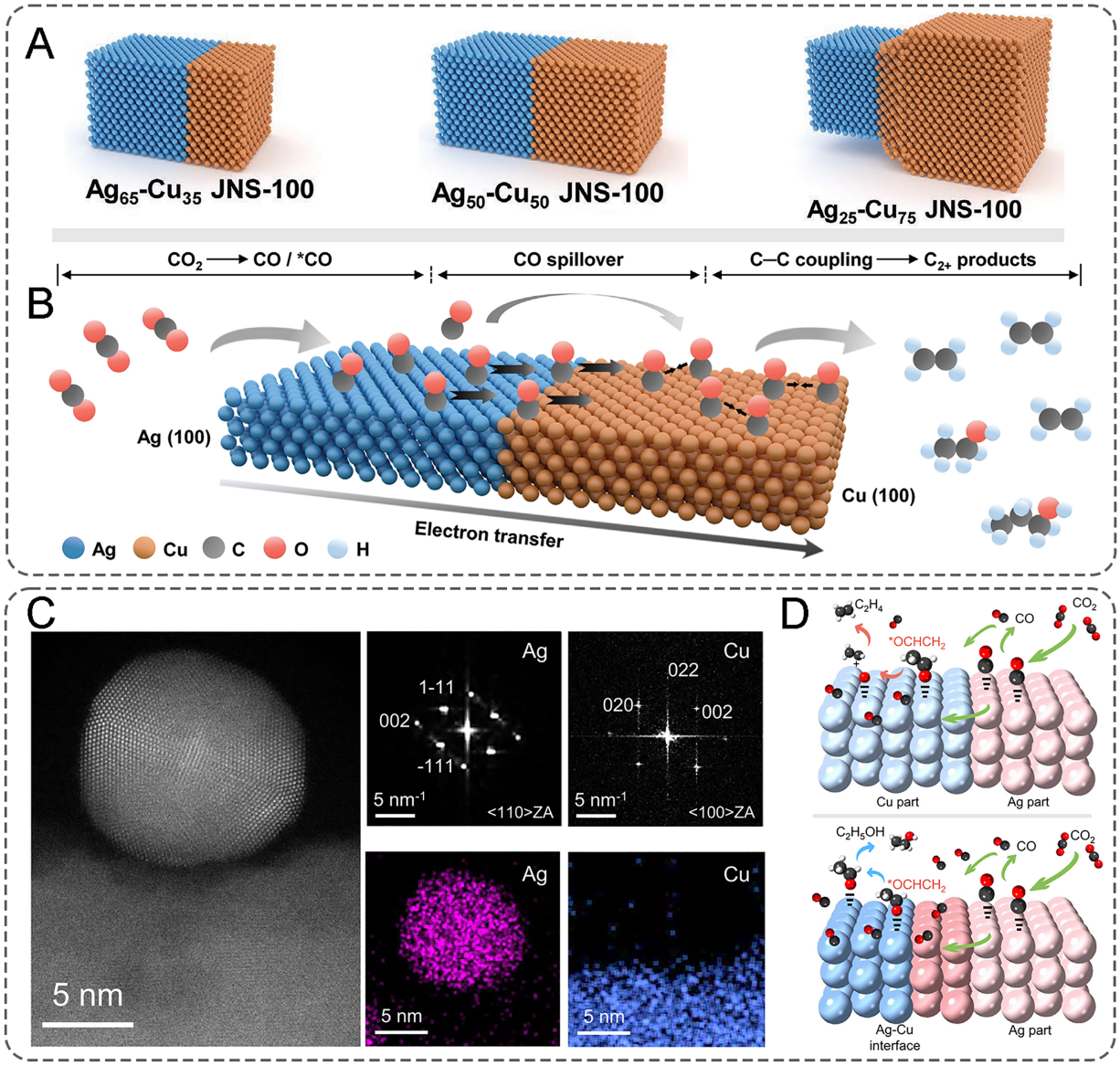


Figure 7. (A) The synthesis of three kinds of Ag-Cu JNS-100 via confined growth of Cu on Ag NCs; (B) Schematic illustration of a plausible eCO_2RR mechanism on Ag_{65}-Cu_{35} JNS-100. (A and B) Reproduced with permission[29]. Copyright 2022, Wiley-VCH; (C) HAADF-STEM images of Ag-Cu biphasic heterostructure (left), FFT patterns taken from Ag and Cu regions in (C) and corresponding EDS elemental maps at Ag-Cu interface; (D) Schematic illustration of the electrocatalytic pathway for C_2H_4 (left) and C_2H_5OH (right). (C and D) Reproduced with permission[69]. Licensed under CC BY-NC-ND 4.0. NCs: Nanocubes; eCO_2RR: Electrocatalytic CO_2 reduction reaction; HAADF-STEM: High-angle annular dark-field scanning transmission electron microscopy; FFT: Fast Fourier transform; EDS: Energy-dispersive X-ray spectroscopy; NPs: Nanoparticles; FEs: Faradaic efficiencies. JNS: janus nanostructures.

For oxygenated products such as ethanol, it is also necessary to determine whether the secondary metal influences the first C-C coupling step or the subsequent oxygen-retention step[24]. If the total C_2 rate remains largely unchanged while the ethanol-to-ethylene ratio increases, this suggests modulation of the adsorption of oxygenated intermediates and C-O bond cleavage; if CO and all C_2 products increase simultaneously, *CO supply is likely the dominant factor. Analysis based on product-specific partial current densities and surface *CO coverage, rather than FE alone, avoids artifacts caused by changes in total current[1]. Notably, a high total C_{2+} FE frequently conceals divergent product branching rather than a single dominant product. For example, framework-regulated pentyl-CuCP delivers a total C_{2+} FE of 73.4% ± 2.9% with an ethylene FE of 40.9% ± 1.2% at 260 mA cm^{-2}[151]. In bimetallic nanowire catalysts, single-atom Ag_1Cu nanowires achieve an

ethanol FE of 56.3% with an ethanol-to-ethylene ratio of 4.26, whereas nanoparticle-decorated AgCu nanowires promote ethylene formation with an FE of 54.9% and an ethanol-to-ethylene ratio of 0.41[67]. Reporting product-specific FE and partial current densities alongside total C_{2+} FE is therefore essential to clarify whether a catalytic strategy directs the reaction toward a specific target molecule.

Microenvironment modulation

Microenvironment modulation reconfigures the reaction network by altering local CO_2, CO, H_2O, OH^-, and cation activities, without necessitating substantial changes to the Cu lattice itself[79,80,152,153]. Confined structures can prolong intermediate residence times; surface molecules can modulate the electric field, wettability, as well as hydrogen bonding; and the electrode-electrolyte structure governs three-phase mass transport[151,154,155]. Analogous to crystal facets or oxidation states, microenvironment optimization is subject to trade-offs: Overly thick overlayers block adjacent Cu sites, insufficient water activity limits proton transfer, and excessive hydrophobicity reduces ion accessibility[156,157]. Therefore, evaluations should simultaneously compare FE, partial current densities, and stability, rather than ascribing performance improvements exclusively to contact angle or bulk pH.

Confinement effect

Carbon-layer confinement can simultaneously enhance ethanol selectivity and structural stability. Wang *et al.*[14] coated Cu with a nitrogen-containing carbon layer, which steered the pathway toward ethanol by suppressing deoxygenation after C-C coupling, achieving a total C_{2+} FE of 93% at 300 mA cm^{-2}, corresponding to an ethanol selectivity of 52% ± 1% and an ethanol partial current density of 156 ± 3 mA cm^{-2}; the ECSA-normalized ethanol partial current density was 1.8-fold higher than that of bare Cu. Kim *et al.*[112] reported Cu NPs protected by a quasi-graphitic carbon shell that attained a C_{2+} FE of 82.3% and a C_{2+} partial current density of 329.2 mA cm^{-2}, and sustained CO_2-to-ethylene conversion for 180 h, whereas unprotected Cu underwent significant reconstruction within hours [Figure 8A-C].

Confining dual-metal tandem sites within a mesoporous architecture provides an effective strategy to regulate intermediate residence times. Zhang *et al.*[158] encapsulated Cu and Ag NPs within mesoporous nanospheres derived from self-polymerized dopamine using a dual-phase template and gas-phase reduction method, achieving uniform spatial confinement of metallic sites within mesopores as evidenced by TEM [Figure 8D]. When evaluated in an H-type cell with 0.1 M $KHCO_3$ under identical metal loadings, CuAg@MSN-3 exhibited outstanding multi-carbon selectivity across a wide potential range (-0.9 to -1.5 V *vs.* RHE), delivering a peak C_2 FE of 75.4% at -1.4 V *vs.* RHE, which substantially exceeds the 30.1% achieved by the unconfined carbon-supported counterpart CuAg/xc-72 [Figure 8E]. *In situ* attenuated total reflection Fourier transform infrared spectroscopy CO-desorption measurements reveal that the mesoporous channels prolong the local CO retention time to 10 min for CuAg@MSN-3 compared to 7 min for Cu@MSN, 6 min for Ag@MSN, and only 2 min for CuAg/xc-72 [Figure 8F]. This extended residence time enriches local *CO concentration and enhances *CO re-adsorption, thereby increasing intermediate coverage on neighboring Cu sites and promoting C-C coupling.

Porous coordination frameworks and three-dimensional electrodes further extend confinement to high-current-density operation. The CuBPZ-CH_3 metal-azole framework achieved a C_{2+} FE of 52.5% and a total current density of 660 mA cm^{-2} at -1.2 V *vs.* RHE, whereas its electronically distinct counterpart CuBPZ-NO_2 yielded only a C_{2+} FE of 20.8%; CuBPZ-CH_3 maintained stable operation for over 70 h[160]. Separately, Bi *et al.*[159] constructed a three-dimensional Cu-chitosan-gas diffusion layer (GDL) (3D Cu-CS-GDL) electrode using chitosan as a transition layer, followed by electrochemical reduction, electrodeposition, and *in situ* reconstruction to form hexagonal-prismatic Cu microrods [Figure 8G]. The resulting hexagonal-prismatic Cu microrods showed a contact angle of 95.1° and close integration with the GDL

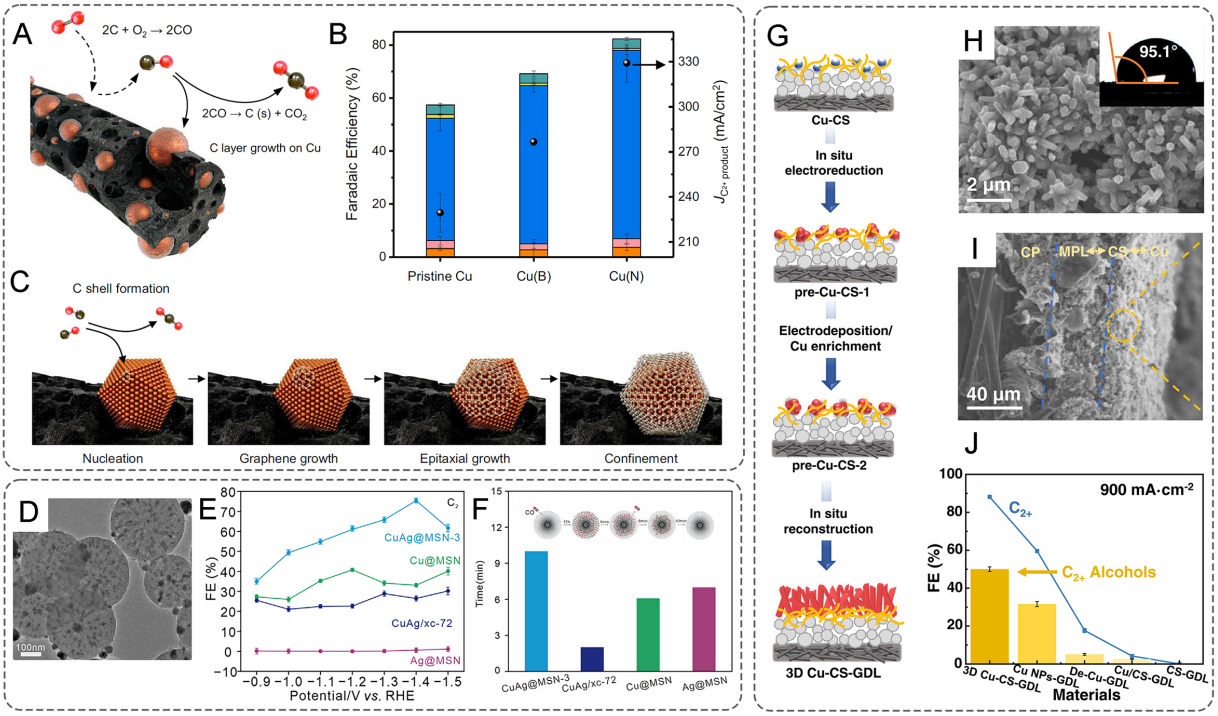


Figure 8. (A) Schematic illustration of the CO-mediated reaction in the Cu-C-O system. The C matrix was nanocarved, forming inner pores by C combustion and generating CO-confined Cu nanoparticles in a quasi-graphitic C shell. The dotted line shows nanocarving, and the solid line shows the Boudouard reaction; (B) FE and partial current density for C_{2+} products at 400 mA cm^{-2}; (C) Formation mechanism of the quasi-graphitic C shell on Cu nanoparticles through the disproportionation of CO. (A-C) Reproduced with permission[112]. Licensed under CC BY 4.0; (D) The TEM image of the CuAg@MSN sample; (E) The FE of C_2 products on CuAg@MSN-3, Cu@MSN, Ag@MSN and CuAg/xc-72 catalysts; (F) The retention times of CO in CuAg@MSN-3, Cu@MSN, Ag@MSN and CuAg/xc-72 catalysts. (D-F) Reproduced with permission[158]. Licensed under CC BY 4.0.; (G) Schematic of the preparation of the 3D Cu-CS-GDL electrode; (H) top-view SEM image and water-contact-angle measurement; (I) cross-sectional SEM image of the 3D Cu-CS-GDL electrode; (J) FEs of C_{2+} products and C_{2+} alcohols over different GDEs. (G-J) Reproduced with permission[159]. Licensed under CC BY 4.0. FE: Faradaic efficiency; TEM: Transmission electron microscopy; SEM: Scanning electron microscopy; GDL: Gas diffusion layer.

[Figure 8H and I]. At 900 mA cm^{-2} and -0.87 V *vs.* RHE, the electrode delivered a C_{2+} FE of 88.2% and a C_{2+} alcohol FE of 51.4%, corresponding to a partial current density of 462.6 mA cm^{-2} [Figure 8J].

Surface modification

Molecular or polymer modification of Cu-based catalysts can regulate product distribution by tuning diffusion behavior and reactant adsorption strength, which promotes CO_2 activation while influencing reaction pathways and energy barriers[80,154]. Organic modification can alter the reaction network on Cu through coordination, hydrogen bonding, interfacial charge, and wettability[151,161,162]. Histidine-modified Cu maintained a maximum C_{2+} FE of 76.6% across a potential window exceeding 1 V, while the C_{2+} partial current density increased by more than 20-fold relative to unmodified Cu and stable operation was maintained for 48 h [Figure 9A][32]. Polymer-anchored pyridine poly-4-vinylpyridine (P4VP) increased the C_{2+} FE to 47.1% ± 3.9% at 60 mA cm^{-2}, more than three times the value for bare oxide-derived Cu; at 220 mA cm^{-2}, the C_{2+} FE reached 71.8% ± 4.3% for P4VP-modified Cu versus 54.9% ± 3.1% for bare oxide-derived Cu, while maintaining approximately 65% C_{2+} FE for 30 h [Figure 9B-E][155].

The gain imparted by the same modifier differs across Cu morphologies. A Schiff-base network increased the ethylene FE by approximately 2.0-, 5.5-, and 5.2-fold for cubic, spherical, and tetrahedral Cu, respectively, with the Cu(200)-rich cubic Cu reaching an ethylene FE of 71.2% ± 2.0% and a current density of 265 mA cm^{-2}, although the ethylene FE subsequently decreased from 71.2% to 61.3% after 24 h

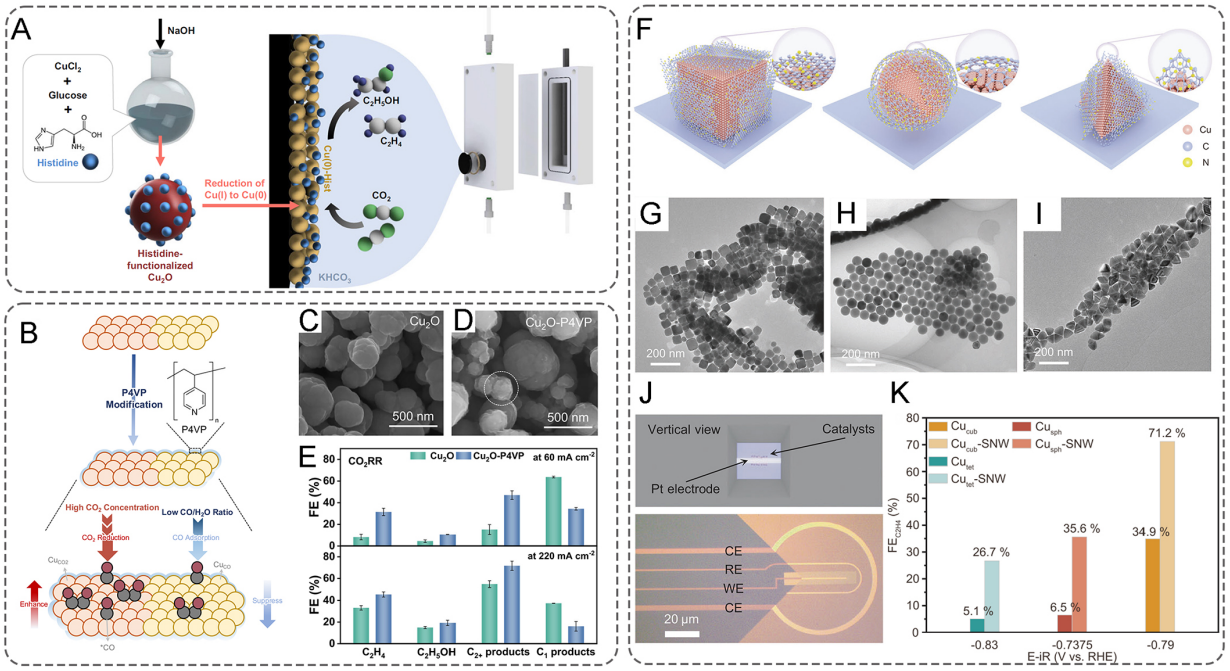


Figure 9. (A) Preparation of histidine-functionalized Cu_2O and its subsequent use in eCO_2RR. (A) Reproduced with permission[32]. Licensed under CC BY 4.0; (B) Schematic diagram of the impact of P4VP on the C_{2+} formation activities of the two distinct Cu sites; SEM images of (C) Cu_2O and (D) Cu_2O-P4VP; (E) FEs of C_1 (CO and formate) and C_{2+} products for Cu_2O and Cu_2O-P4VP in the eCO_2RR at 60 and 220 mA cm^{-2}, respectively. (B-E) Reproduced with permission[155]. Licensed under CC BY-NC-ND 4.0; (F) Structural models of Cu_{nps} and Cu_{nps}-SNW; TEM images of (G) Cu_{cub}, (H) Cu_{sph}, and (I) Cu_{tet}, respectively; (J) Layout of single-particle electrochemical platform with microelectrodes for eCO_2RR; (K) C_2H_4 FE values for Cu_{nps} and Cu_{nps}-SNW at different potentials. (F-K) Reproduced with permission[154]. Licensed under CC BY-NC-ND 4.0. SEM: Scanning electron microscopy; NW: Nanowire; TEM: Transmission electron microscopy; FE: Faradaic efficiency; NPs: Nanoparticles; eCO_2RR: Electrocatalytic CO_2 reduction reaction.

[Figure 9F-K][154]. Cu modified with a fluorine-containing hydrophobic polymer in an MEA increased the C_{2+} FE from 61.59% for bare Cu to 71.08%, with a C_{2+} partial current density of 355.4 mA cm^{-2}, while simultaneously suppressing H_2 evolution[163]. These morphology-dependent responses indicate that the effect of the molecular layer depends on the underlying crystal facet and mass-transport conditions.

To establish causality, molecular modification studies should compare structurally analogous molecules at identical coverage and contact angle. If C_{2+} selectivity varies only with wettability, the effect is most likely attributable to CO_2/H_2O mass transport; only when selectivity changes with the anchoring group or electron-donating/withdrawing substituent at comparable wettability can a direct intermediate or valence-state mechanism be invoked[32,154]. The persistence of the molecular overlayer and ECSA should also be reported, because the overlayer may either stabilize Cu or block contiguous Cu sites[155].

Electrode-electrolyte interface engineering

Local alkalinity, cations, anions, water activity, and wetting state collectively constitute the electrode-electrolyte interface, and interface-induced performance variations can far exceed material-intrinsic effects[164-166]. Larger alkali-metal cations can stabilize dipolar or negatively charged intermediates via the interfacial electric field while enhancing *CO coverage; Monteiro *et al.*[33] found that in metal-cation-free electrolytes, no detectable CO_2 reduction occurs on Cu, Au, or Ag, indicating that partially desolvated cations play an essential role in stabilizing early CO_2^--type intermediates. Anions modulate pH buffering, participate in specific adsorption, and may induce Cu reconstruction. Identical bulk pH does not guarantee identical interfacial conditions: At high current densities, the reaction-diffusion balance generates substantial gradients[167-171].

Engineering an abrupt alkaline interface demonstrates the synergy between local OH^- and CO_2 flux. Dinh *et al.*[10] constructed an abrupt alkaline interface between Cu and a hydrophobic layer, achieving an ethylene FE of 70% and maintaining stable operation for 150 h in a flow cell [Figure 10A-D], while sustaining high selectivity at -0.55 V *vs.* RHE; experiments and calculations attributed the performance enhancement to interfacial OH^- reducing the barriers for CO_2 reduction and *CO-*CO coupling. The key innovation is not merely the use of 10 M KOH, but the establishment of high OH^- concentration near Cu combined with shortened gas diffusion distance. Raising only the bulk alkalinity would induce CO_2 carbonation and potentially lower carbon utilization; therefore, local alkalinity must be evaluated jointly with the reactor carbon balance[173,174].

Ionomer bilayers can independently regulate the CO_2/H_2O ratio and local pH. A Nafion/Sustainion bilayer increased the C_{2+} FE from 61% to 80% while suppressing H_2 evolution from 18% to 5%; combination with pulsed electrolysis enhanced the C_{2+} partial current density by 250% relative to static bare Cu, with a total C_{2+} FE of 90% and H_2 at only 4%[164]. Rashid *et al.*[172] compared a commercial anion-exchange-membrane electrode with bilayer ionomer configurations [Figure 10E-G]. Infusing the Nafion layer with KOH further increased C_{2+} production: the optimized bilayer reached a C_{2+} partial current density of approximately 284 mA cm^{-2} at a total current density of 350 mA cm^{-2} [Figure 10H]. However, at high current densities, ionomers develop through-plane ion and pH gradients and may delaminate or restrict mass transport[173]. Therefore, the performance gains of bilayer structures are not universally applicable across all membrane thicknesses and water contents.

IN SITU CHARACTERIZATION AND THEORETICAL SIMULATION

The pre-reaction structure of Cu-based catalysts can only describe the starting point of the reaction and cannot represent the true active state during C_{2+} product formation[13]. Under the concerted action of cathodic bias, adsorbates, and the local electric field, Cu undergoes valence-state reduction, facet rearrangement, defect formation, particle migration, and redeposition; concurrently, the coverages of *CO, OH^-, and oxygen-containing C_2 intermediates evolve continuously[48]. This chapter follows the progression from "static structure" through "operando evolution" to "dynamic reaction network": *In situ* and operando characterization captures structural and intermediate changes over time; DFT compares candidate sites and elementary steps; and microkinetic modeling translates energies, coverages, and mass transport into measurable product-specific rates. These three approaches are not interchangeable but rather complement one another in sequentially reducing uncertainty regarding the true structure and reaction pathway[25,62,69,77,95,96,99,117]. Here, a working-state active site is defined as the potential- and environment-dependent atomic ensemble that exists during catalytic turnover and directly governs a measurable elementary step; it includes the local Cu coordination and valence environment together with the relevant adsorbate coverage, rather than the as-synthesized structure alone.

In situ characterization

Conventional *ex situ* characterization is typically performed under open-circuit, potential-off, or ambient conditions. It is therefore suitable for confirming precursor composition and overall post-reaction changes, yet prone to missing rapid reduction, short-lived species, and reversible reconstruction. For example, the detection of Cu^+ by post-reaction XPS does not prove that Cu^+ persistently participates in turnover at the target potential; similarly, the observation of Cu(100) cubes before reaction does not guarantee that intact terraces are preserved under high current densities[25,62,63,97-100]. The core value of *in situ* characterization lies in recording structure while applying potential and maintaining reactant supply[175]; operando characterization further requires that the catalyst layer, flow rate, electrolyte, and current density approach actual working conditions as closely as possible.

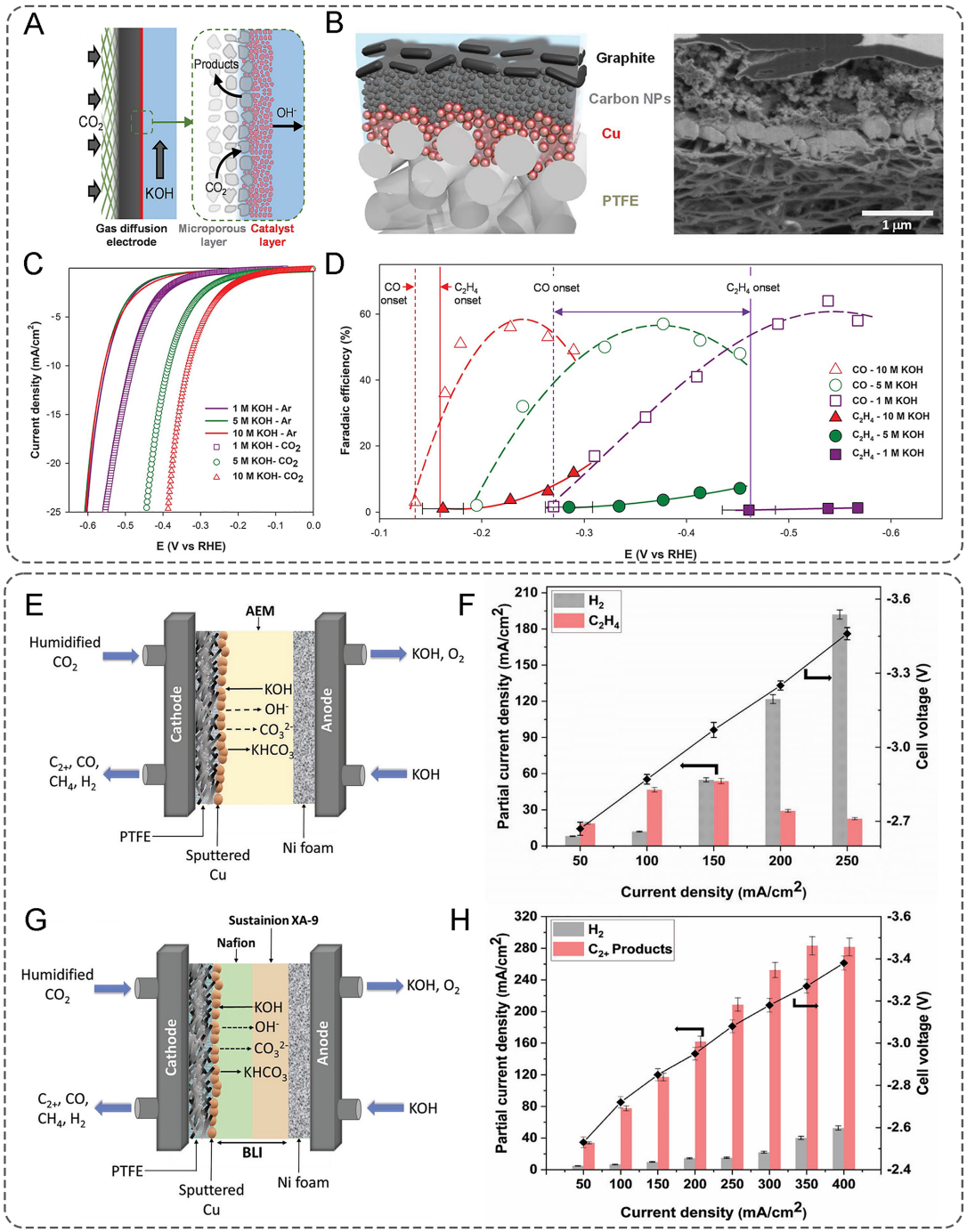


Figure 10. (A) Schematic of the cathode portion of a gas diffusion electrode for CO_2; (B) Schematic illustration and Cross-sectional SEM image of the graphite/carbon NPs/Cu/PTFE electrode, (C) LSV scan in various KOH electrolytes; (D) C_2H_4 and CO FEs with increasing KOH concentrations. (A-D) Reproduced with permission[10]. Copyright 2018, AAAS; eCO_2RR using Sustainion X37-50 Grade RT AEM and 1 M KOH as anolyte: (E) schematic diagram of the MEA system; (F) partial current density of C_2H_4 and H_2 and cell voltage at different current density; (G) schematic diagram of the MEA system using BLI-25:25 on Cu catalyst in reverse bias mode; (H) partial current density toward C_{2+} and H_2 at different current density; using 100 mL of 1 M KOH as anolyte. (E-H) Reproduced with permission[172]. Licensed under CC BY 4.0. LSV: Linear sweep voltammetry; FEs: Faradaic efficiencies; eCO_2RR: Electrocatalytic CO_2 reduction reaction; AEM: Anion exchange membrane; MEA: Membrane electrode assembly; BLI: Bilayer ionomer. PTFE: polytetrafluoroethylene.

In situ Raman and infrared spectroscopy are well suited for identifying surface adsorbates. SERS can cover low-wavenumber vibrations such as Cu-O and Cu-ligand modes, and the Raman scattering of water is relatively weak[71,176]. By contrast, surface-enhanced infrared absorption spectroscopy and attenuated total

reflection infrared spectroscopy are more sensitive to *CO, *OCCO, and oxygen-containing intermediates. Both techniques can track changes in peak intensity and position as a function of potential, yet peak intensity is not equivalent to surface coverage, because enhancement factors, molecular orientation, and the local electric field all influence the signal. By combining SERS, isotope labeling, and DFT analysis, Zhan *et al.*[20] found that undercoordinated Cu sites more readily form *OC-CO(H) intermediates associated with the ethylene pathway, whereas highly compressed and distorted Cu domains favor the ethanol pathway. Herzog *et al.*[71] employed sub-second operando Raman spectroscopy to study pulsed CO_2 reduction and found that moderate co-adsorption of OH^- and *CO promotes ethanol formation [Figure 11A]; low OH^- coverage favors C_1 products, whereas excessively high coverage suppresses C-C coupling. These results indicate that the mere appearance of a spectral peak is only the first step; the critical challenge is to correlate peak positions, isotopic shifts, and coverage changes synchronously with product-specific rates.

Complementing these spectroscopic approaches, microscopic methods have revealed the transformation of Cu morphology from static particles to a dynamic nanocrystalline network. Using operando electrochemical liquid-cell STEM, 4D-STEM, and time-resolved X-ray absorption spectroscopy (XAS), Yang *et al.*[97] found that 7 nm Cu particles coalesce during electrolysis into grain-boundary-rich metallic Cu nanocrystallites; the sample with an active nanocrystallite fraction approaching unity exhibited a sixfold higher C_{2+} selectivity relative to 18 nm samples with a nanocrystallite fraction of approximately one-third. In a separate Cu-nanowire study, Yang *et al.*[177] directly observed nanograin nucleation during the first 20 s of operando liquid-cell EC-STEM imaging, followed by Cu migration and fragmentation of the spongy Cu shell between 20 and 40 s [Figure 11B]. Complementary 4D-STEM identified differently oriented grains and their boundaries in the reconstructed metallic Cu. Grosse *et al.*[101] observed that Cu cubes undergo fragmentation, desorption, and re-deposition to form particle networks of differing stability [Figure 11C]; over 12 h, the C_{2+} FE of the 170 nm sample decreased by 24%, whereas the 390 and 80 nm samples exhibited decreases of 46% and 54%, respectively. These results indicate that the initial size and morphology must be reinterpreted through the working-state particle distribution. Liquid-phase TEM and electrochemical scanning probe techniques can directly observe particle migration, dissolution, agglomeration, and local activity differences, providing spatial information on the dynamic reconstruction of Cu. Nevertheless, "*in situ*" does not automatically equate to "authentic operating conditions". A more credible approach is to combine XAS with vibrational spectroscopy in the same reactor at current densities close to the target value, with concurrent online product analysis; if full co-location in a single cell is not feasible, the catalyst layer, flow rate, electrolyte, and potential protocol should at least be kept consistent.

X-ray techniques extend structural characterization to crystal phase, valence state, and local coordination. XAS can track the average oxidation state and electronic structure via X-ray absorption near edge structure, and yields local coordination numbers and bond lengths via extended X-ray absorption fine structure, rendering it well suited for examining Cu_2O reduction, Cu-Cu coordination formation, and bimetallic interface evolution. Its limitation lies in its large penetration depth and bulk-averaged signal, so that minor surface-active species may be overwhelmed by the bulk signal. De Ruiter *et al.*[25] employed wide-angle X-ray scattering and small-angle X-ray scattering to observe that Cu_2O is fully converted to metallic Cu within 40 s of applying cathodic bias, followed by coarsening and increased bridging *CO, accompanied by a decline in C_2 hydrocarbon selectivity over ~30 min. Vavra *et al.*[135] detected soluble Cu^+ carbonyl species, which belong to transient intermediates in the dissolution-migration-redeposition process rather than stable lattice sites. Attribution of dynamic processes also depends on time resolution. Cu_2O reduction and particle migration can occur within seconds, pulsed adsorbates vary on sub-second timescales, whereas liquid products are typically integrated over several minutes[71].

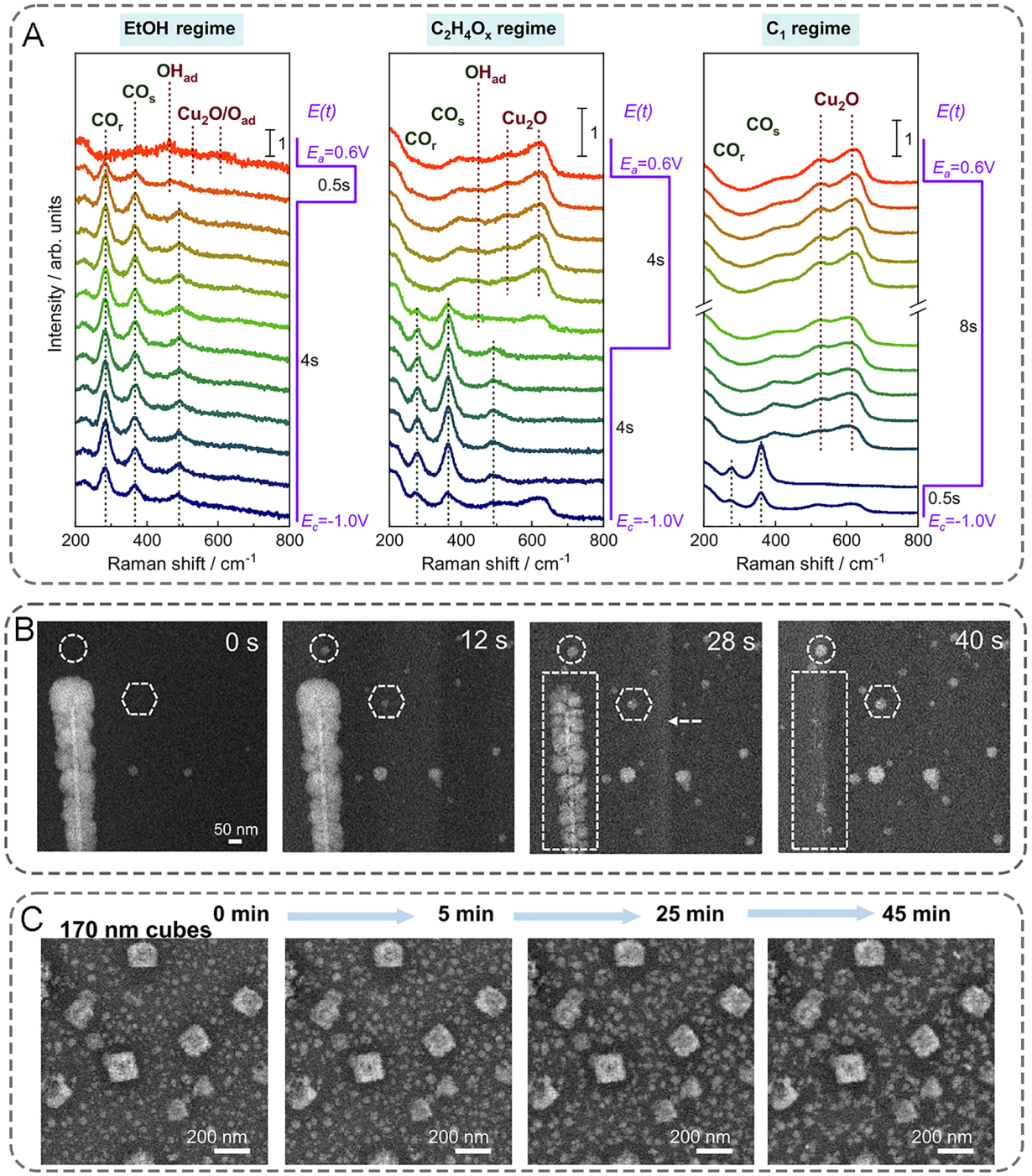


Figure 11. (A) Normalized SERS spectra from bottom to top with highlighted characteristic SERS bands during pulsed eCO_2RR with varying pulse lengths. (A) Reproduced with permission[71]. Licensed under CC BY 4.0; (B) Operando EC-STEM images of dynamic evolution of Cu NWs, nucleation of initial growth of Cu nanograins from a metallic Cu NW core surrounded by the spongy Cu shell (Cu@CuS) from 0 to 20 s with two Cu nanograin seeds in dashed boxes; significant Cu migration from Cu NWs to form Cu nanograins at adjacent locations from 20 to 40 s. (B) Reproduced with permission[177]. Copyright 2024, American Chemical Society; (C) Snapshots extracted from the videos tracking the evolution of 170 nm cubes at 0, 5, 25, and 45 min after applying a potential of -0.9 V *vs.* RHE by EC-TEM. (C) Reproduced with permission[101]. Licensed under CC BY 4.0. SERS: Surface-enhanced Raman spectroscopy; eCO_2RR: Electrocatalytic CO_2 reduction reaction; EC-STEM: Electrochemical scanning transmission electron microscopy; LSV: Linear sweep voltammetry; CA: chronoamperometry.

In situ XRD is advantageous for identifying crystal phases and average grain-size changes, yet it struggles to detect amorphous layers and low-concentration species. The transition from a single *in situ* technique to multimodal correlative characterization is a necessary development for identifying dynamic active sites.

Surface-enhanced spectroscopy emphasizes local hotspots; XAS reflects the average coordination within the irradiated volume; XRD is sensitive only to long-range ordered phases; and electron microscopy can observe only a limited field of view. Applying spectroscopy, microscopy, and diffraction to the same pulsed Cu(100) system, Tanase *et al.*[95] found that (n10) facets, surface or subsurface oxide species, and an ultrathin metallic layer form simultaneously, each of which may influence ethylene and ethanol selectivity. Therefore, discrepancies among multimodal results are not necessarily contradictory; one should first compare probing depth, detection limit, and sampling region before judging whether they describe the same working-state structure.

DFT

The development of first-principles methods for simulating electrochemical reactions has made it possible to investigate reaction mechanisms theoretically and to inform catalyst design. DFT provides atomic-scale interpretation of static experimental structures; the most common application is to compare adsorption configurations, reaction free energies, and transition states on ideal crystal surfaces[169]. The computational hydrogen electrode model links the chemical potential of proton-electron pairs to the applied potential, thereby enabling rapid comparison of pathways such as *CO dimerization, *CO hydrogenation, and post-coupling deoxygenation[12,13]. Such static energy diagrams are suitable for screening clearly unfavorable steps, but cannot directly yield operando coverages or product formation rates. In particular, when two pathways differ by only 0.1-0.3 eV, uncertainties in the choice of functional, dispersion correction, coverage, and solvation treatment may alter the predicted pathway hierarchy[48]. Static DFT therefore provides candidate mechanisms rather than definitive ones.

The transition from static surface models to a dynamic electrochemical interface requires explicit consideration of potential, solvent, and the electric double layer[170]. Implicit solvation models allow continuous variation of the surface charge but cannot describe explicit hydrogen-bonding networks or water participation in the reaction; explicit-solvent ab initio molecular dynamics (AIMD) can resolve the local water network but remains limited by cell size and sampling time. Zhang *et al.*[43] employed explicit-solvent AIMD to demonstrate that alkali-metal cations, *CO_2, and interfacial water collectively stabilize the early activation configuration, a finding consistent with the experimental observation that no CO_2 reduction is detected on Cu in the absence of metal cations [Figure 12A and B]. Constant-charge models additionally suffer from potential drift arising from work-function changes upon adsorption and reaction; accordingly, charged intermediates and transition states are more appropriately described within a constant-potential or grand-canonical framework[13,33].

Operando characterization also reshapes the structural models adopted in DFT calculations. Using pre-reaction Cu_2O, Cu NCs, or bimetallic alloys directly as computational starting points risks overlooking rapid reduction, adsorption-induced faceting, and elemental migration[25,51,69]. Single-crystal facet studies have established a relatively complete predictive-validative cycle: Cu(100)/Cu(111) interface models predict that such boundaries enhance *CO adsorption and lower the C-C coupling barrier, a prediction subsequently corroborated by a C_{2+} FE of 74.9% ± 1.7% at 300 mA cm^{-2}[65]; calculations incorporating co-adsorbed CO/OH^- further predict the formation of Cu(100)-rich surfaces, which was verified by *in situ* faceting experiments and ultimately led to a C_{2+} FE of 83% at 500 mA cm^{-2}[51]. At this stage, the computational object is no longer the as-synthesized facet but the experimentally confirmed operando structure.

Studies on defect and bimetallic systems demonstrate that dynamic models must encompass multiple sites and the migration of intermediates. Calculations on Cu_2S-Cu vacancy systems indicate that vacancies and subsurface sulfur primarily alter the oxygen-retention versus deoxygenation branching following C-C coupling, consistent with a C_{2+} alcohol FE of 32% ± 1% and a partial current density of 126 ± 5 mA cm^{-2}[24];

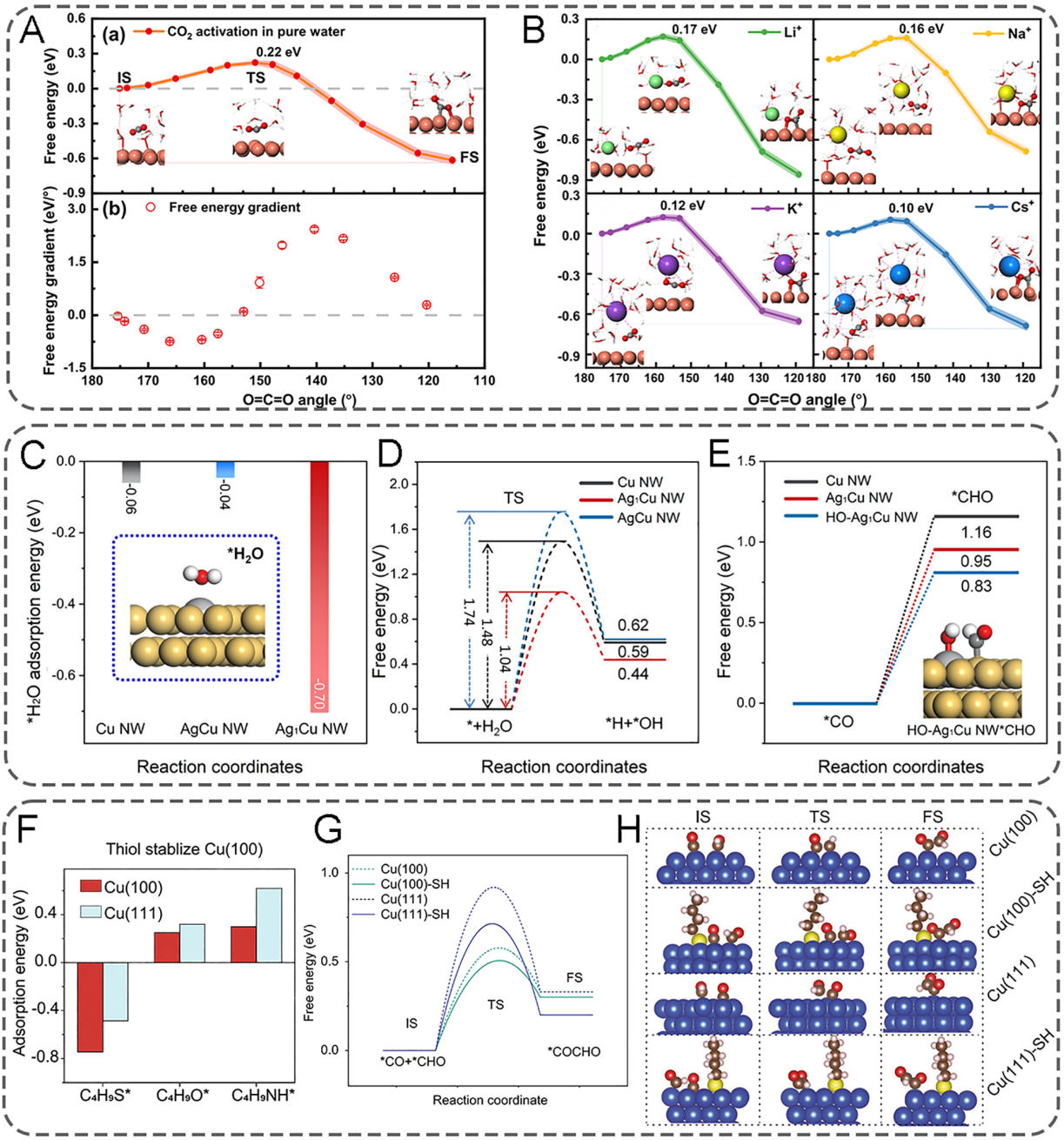


Figure 12. (A) Free energy profile and representative IS, TS, and FS structures for the CO_2 adsorption process in the pure water system without M^+; (B) Free energy profiles and representative structures at IS, TS, and FS for CO_2 adsorption with different cations of Li^+, Na^+, K^+, and Cs^+. (A and B) Reproduced with permission[43]. Licensed under CC BY 4.0; (C and D) The adsorption and dissociation energies of H_2O on Cu NW, AgCu NW and Ag_1Cu NW. (E) Gibbs free energy diagrams for *CO hydrogenation to *CHO over Cu NW, Ag_1Cu NW and HO-Ag_1Cu NW. (C-E) Reproduced with permission[67]. Licensed under CC BY-NC-ND 4.0. (F) DFT calculations of the adsorption energies of various alcohols, thiols, and amines with alkyl chains; The free energy diagram (G) and optimized structures (H) of the CO-CHO coupling process on the Cu(100), Cu(100) with $*C_4H_9S$, Cu(111) and Cu(111) with $*C_4H_9S$ surfaces. (F-H) Reproduced with permission[178]. Licensed under CC BY 4.0. NW: Nanowires; IS: initial state; TS: transition state; FS: final state; DFT: Density functional theory.

grain-boundary models propose that adjacent regions sequentially mediate CO generation, coupling, and subsequent reduction[31]. In bimetallic systems, Cu decorated with Ag NPs and Ag single-atom alloys favor ethylene and ethanol, respectively, as operando spectroscopy, isotope experiments, and DFT have linked the difference to *COCO- and *COCHO-related pathways [Figure 12C-E][67]. These systems cannot be described by a single adsorption energy; site adjacency, coverage, and species diffusion must also be incorporated.

Organic modification and the local microenvironment further expand the configurational space of the dynamic interface. Aryl diazonium salt functionalization establishes a continuously tunable series of $Cu^{\delta+}$ states; the computationally predicted valence-ethylene trend was corroborated by synthesis and MEA testing, with the optimal sample reaching an ethylene FE of 83% ± 2% and an ethylene partial current density of 212 mA cm^{-2}[130]. Another surface-modification route was demonstrated by Yao *et al.*[178], who selected a thiol modifier because calculations indicated stronger adsorption on Cu(100) than on Cu(111) [Figure 12F]. Their model further showed a lower *CO-*CHO coupling barrier on Cu(100), with thiol adsorption reducing that barrier by approximately 0.07 eV [Figure 12G and H]. Reducing the water activity from 0.97 to 0.72 raises the C_2 FE from 10% to 66% and increases the current approximately threefold, indicating that changes in the water network and surface coverage can simultaneously rearrange the reaction landscape[45]. For such systems, a physically meaningful model would need to sample multiple ligand orientations, surface coverages, and solvent arrangements rather than relying on a single lowest-energy configuration.

The evolution of DFT from static to dynamic does not imply that models can be made arbitrarily complex; rather, each added layer of complexity must address a testable question. High-level embedded cluster calculations can correct the bias of commonly used functionals toward CO/Cu adsorption sites[48]; constant-potential models can examine the potential response of charged transition states; and AIMD can predict the instantaneous structure of cations or water networks. Theoretical predictions should be translated into isotope effects, peak shifts, reaction orders, or turning points in product ratios, for subsequent experimental verification. If different reasonable models yield opposite orderings, or if the results are highly sensitive to coverage and solvation, uncertainty intervals should be reported, and researchers should explicitly acknowledge that current calculations cannot yet distinguish between candidate pathways.

Microkinetics

Static free-energy diagrams can identify thermodynamically favorable steps but cannot directly indicate which step controls the rate at a given potential and coverage. Microkinetic modeling combines adsorption equilibria, elementary reaction rates, and site conservation to compute steady-state coverages and product-specific formation rates. For Cu-based C_{2+} reactions, the model must minimally include the pathway from CO_2 to *CO, *CO desorption and re-adsorption, various C-C coupling channels, hydrogen evolution, the methane pathway, and the ethylene/ethanol branching[2,13]. Because potential, local pH, and CO partial pressure simultaneously alter multiple steps, no single step remains rate-determining across all conditions.

The transition from mean-field microkinetics to a dynamic surface requires consideration of coverage-dependent interactions, surface diffusion, and site size. Li *et al.*[47] employed kinetic Monte Carlo simulations to study the diffusion of carbon-containing intermediates on Cu surfaces and used isotope mixing responses to constrain the surface ensemble required for C-C coupling. Experimentally, the conversion from CO_2 to CO and from CO to C_{2+} products proceed on different Cu sites, and subsequent C_{2+} conversion on CO-rich sites is enhanced by approximately sixfold[21]. These findings demonstrate that models should not rely solely on low-coverage adsorption energies but must also incorporate *CO interactions, site blocking, and the probability of *CO migrating from generation sites to coupling sites.

The dynamic variation of potential and microenvironment requires that models be established jointly with systematic condition-variation experiments. Reducing the water activity from 0.97 to 0.72 increased the C_2 FE from 10% to 66% and approximately tripled the current density; the product-specific reaction orders for the C_1, C_2, and H_2 pathways also changed markedly as a function of water activity[45]. Pulsed electrolysis periodically alters *OH, *CO, and the Cu surface state[71]. These data can test whether the performance enhancement originates from increased *CO coverage, altered proton transfer, or structural regeneration. Only when a model reproduces the FE, product-specific partial currents, reaction orders, and dynamic

responses does it possess greater mechanistic discriminatory power than merely fitting a single polarization curve.

Under high-current conditions, surface reactions must be integrated with mass transport within the catalyst layer. Adesina *et al.*[173] combined DFT, acid-base equilibria, and multiscale transport to predict that through-plane gradients of K^+, carbonate, pH, and potential develop within the Nafion layer. In dual-layer ionomer experiments, the C_{2+} FE increases from 61% to 80%; combination with pulsing further raises this to 90% while suppressing H_2 to 4%[164]. This demonstrates that the local CO_2/H_2O ratio and pH can significantly alter the apparent kinetics. In zero-gap electrolyzers, even a change in anolyte KOH concentration can shift the cathode products from CO-dominated to ethylene/H_2-dominated through cation crossover across the membrane[156]. Therefore, device-level transport cannot be reduced to a vague "effective barrier".

The goal of microkinetic modeling is to form a predictive and correctable reaction network under dynamic conditions. CO versus CO_2 feed comparisons can distinguish upstream CO generation from subsequent C_2 conversion[57]; isotope mixing can constrain surface diffusion[47]; and water activity and pulse frequency separately perturb solvation and transient coverage. A more complete iterative workflow should proceed as follows: Operando characterization provides the working-state structure, DFT generates candidate steps and energy ranges, microkinetics predicts the response of multiple product channels, and new-condition experiments then eliminate models inconsistent with the results. If different networks yield identical predictions for the existing data, multiple possibilities should be retained rather than asserting a unique mechanism based solely on a best-fit curve.

CHALLENGES AND OUTLOOK

Cu is currently the central metal capable of electrochemically reducing CO_2 at appreciable rates to form a variety of C_{2+} products, yet its advantage does not stem from any fixed structure but rather from the synergy between adjacent Cu sites and carbon-containing intermediate coverage, modulated by the local solvation environment under working conditions. The mechanisms described in this review indicate that *CO coverage, the geometric relationship between neighboring Cu sites, local strain, OH^- co-adsorption, and proton supply govern C-C coupling; the subsequent oxygen retention or removal of the coupled intermediate then directs selectivity toward ethanol, ethylene, and other C_{2+} products[12,20,65,71]. Structural regulation can be organized into hierarchical levels: (i) crystal facet and morphology, (ii) defects and valence state, (iii) bimetallic and single-atom alloys, (iv) confinement and molecular interfaces, and (v) the catalyst-layer microenvironment. Operando Cu(100) faceting, Cu^+/Cu^0 interfaces, and geometrically adjacent sites all enhance the probability of C-C coupling. However, bimetallic and confinement designs simultaneously alter the local pH, ion distribution, and mass transport; consequently, structural factors and interfacial factors cannot be discussed in isolation[51,65,67]. *In situ* spectroscopy, XAS, microscopy, and isotope experiments should therefore be cross-validated against DFT, microkinetic modeling, and multiscale transport models, rather than treating a single characterization technique or single-step energy barrier as sufficient causal evidence. From a device perspective, interfacial alkalinity, water activity, cation crossover across the membrane, ionomer, and GDL collectively shape the high-current interface[10,45,156,164]. The demonstration of ethylene operation exceeding 150 h under strongly acidic conditions, together with the C_{2+} performance of ampere-level channeled electrodes, indicates that catalyst design must be integrated with the membrane, electrode pore structure, CO_2 recycling, and product separation[78,153]. In summary, the key to Cu-based C_{2+} electrosynthesis is not the mere superposition of structural features but the establishment of verifiable connections from working-state active sites to product-specific fluxes and further to device-level CE and lifetime. Moreover, significant challenges remain in both the exploration and practical implementation of electrochemical CO_2 conversion to C_{2+} products. We summarize the following outlook to address the current challenges facing electrochemical CO_2-to-C_{2+} conversion.

Causal identification of working-state C-C coupling sites

The central challenge is that pre-reaction descriptors such as crystal facet, defect density, or Cu^+ fraction merely label the precursor; they do not identify the active site operative during C_{2+} formation. Cu_2O is reduced within ~40 s, Cu particles fragment and redeposit, and soluble Cu^+ may exist only as a fleeting intermediate of structural reconstruction. Meanwhile, the surface coverages of *CO, OH^-, and oxygenated C_2 intermediates shift rapidly with applied potential[25,71,97,135]. As a result, a given performance gain can reflect simultaneous changes in site geometry, oxidation state, and local microenvironment. Current evidence is generally sufficient to establish correlation, showing that certain features appear together, but falls short of proving that any single structural motif is causally responsible.

Future studies would benefit from moving beyond static structural comparisons toward dynamic perturbation-and-recovery experiments that can help establish causality. Ideally, this would involve simultaneously tracking working-state structure, intermediate coverages, and product-specific rates on a common time axis, while selectively perturbing candidate sites through potential pulses, compositional gradients, or reversible ligand exchange. A more convincing active-site assignment could be made when the structural change precedes the rate response, performance recovers upon structural restoration, and variations in ECSA, local pH, and mass transport have been accounted for as potential confounding factors. It would also be desirable to resolve stability assessment into distinct phases—startup reconstruction, quasi-steady-state operation, and irreversible failure—so that Cu dissolution, catalyst-layer degradation, and membrane/GDE failure can be quantified independently[26,95].

From total C_{2+} to single-product selectivity and unified evaluation

A high total C_{2+} FE often reflects the combined contributions of multiple product channels—ethylene, ethanol, acetate, and others—each carrying distinct implications for downstream separation costs and product value. It would therefore be beneficial for future studies to report product-specific FE, partial current density, SPCE, and long-term stability concurrently, thereby providing a more comprehensive assessment of CO_2 electroreduction performance.

H-type cells are well suited for mechanistic dissection, whereas flow cells and zero-gap MEAs are designed for high-rate and device-level performance evaluation; the three platforms serve complementary purposes and should not be ranked solely by peak FE. Cross-platform comparisons could be made more meaningful by employing the same catalyst batch, unified potential calibration, and consistent product quantification protocols, with explicit reporting of catalyst-layer loading, ionomer content, membrane type, and CO_2 flow rate.

Moving beyond C-C coupling toward downstream selectivity control is a necessary step if single-product targeting is to be achieved. The ethylene/ethanol ratio can serve as a useful diagnostic for the competition between deoxygenation and oxygen retention, while acetate formation calls for simultaneous consideration of both surface pathways and solution-phase reactions. Confinement effects, oxophilic sites, and local water activity may each be tuned toward specific product branches, though such design strategies would need to be validated through *in situ* spectroscopy, isotopic labeling, and microkinetic modeling.

Deactivation mechanisms across length scales

Beyond activity and C_{2+} selectivity, long-term stability remains a central bottleneck for Cu-based eCO_2RR catalysts. Experimentally, oxide-derived and mixed-valence Cu surfaces often reconstruct under cathodic bias: residual Cu^+/oxide domains are reduced, NPs agglomerate or sinter through migration-coalescence and Ostwald ripening, and the ensembles responsible for *CO adsorption and C-C coupling are altered, shifting products toward CO, H_2, or methane[179]. Analogous dynamic active-site restructuring and

potential-dependent degradation have been reported during alkaline CO reduction[180]. Electrolyte- and operation-related processes may further contribute to performance decay, including metallic impurity deposition, localized carbonate precipitation, and potential catalyst fouling by carbonaceous residues[181]. These pathways are strongly device-dependent because mass transport in H-cells, flow cells, and MEAs affects local pH, *CO coverage, and the balance between restructuring and productive turnover[100].

Theoretically, deactivation is linked to the potential-dependent stability of surface phases and adsorbates. Computational Pourbaix analyses and grand-canonical DFT indicate that Cu^{+}/oxide motifs often invoked for selective C-C coupling may be metastable under strongly reducing conditions, consistent with the frequently observed $Cu^{+} \rightarrow Cu^{0}$ conversion[182,183]. Potential- and adsorbate-dependent reconstruction of Cu(100) can modify the surface ensembles responsible for C-C coupling[184], while evolving adsorption energies of *CO, *H, and oxygenates provide a microscopic basis for selectivity drift. Most DFT models remain static and therefore cannot fully capture coupled reconstruction-reaction kinetics; operando-constrained structural models, microkinetic analyses, and kinetic Monte Carlo simulations that include site conversion—together with explicit treatment of water activity, cations, and carbonate equilibria—are therefore needed[185,186]. Looking forward, rigorous stability studies should report not only FE retention but also time-resolved structural metrics and carbon-efficiency losses so that specific deactivation channels can be correlated with performance decay[181].

Toward standardized performance evaluation across H-cells, flow cells, and MEAs

H-type cells, gas-diffusion flow cells, and zero-gap MEAs operate under markedly different mass-transport characteristics, interfacial ionic environments, and ohmic-loss regimes, and therefore cannot be meaningfully ranked by peak FE alone. H-type cells are limited by the modest aqueous solubility of CO_2 (~30-35 mM) and relatively long diffusion distances, often limiting attainable geometric current densities under ambient, unpressurized conditions. Their well-controlled three-electrode configuration, however, makes them useful for low-current mechanistic and kinetic studies, provided that mass-transport limitations, local pH changes, and iR losses are carefully evaluated. Gas-diffusion flow cells overcome these mass-transfer constraints by delivering gaseous CO_2 through a porous GDE, enabling current densities of hundreds of mA cm^{-2} (and higher in optimized systems). When alkaline or near-neutral liquid catholytes are used, however, parasitic carbonation can consume a substantial fraction of the fed CO_2, promoting salt precipitation, GDE flooding, and elevated ohmic losses. Zero-gap MEAs further reduce transport distances and cell resistance by integrating the catalyst layer directly with an ion-exchange membrane, supporting high-current-density operation (several hundred mA cm^{-2}, and ampere-level in selected systems). Yet their performance remains highly sensitive to membrane properties, hydration, and ionic transport. El-Nagar *et al.*[156] demonstrated that anolyte-derived cation crossover can strongly alter CO_2-reduction selectivity on Cu, while Yu *et al.*[81] showed that enhancing intermediate coverage promotes CO_2 reduction and suppresses HER under acidic conditions, enabling efficient high-rate operation.

These differences necessitate a standardized evaluation framework that separates catalyst-level kinetics from device-level performance. Measurements intended to approximate intrinsic kinetics should be performed under well-calibrated three-electrode conditions with appropriate potential calibration and iR correction, while explicitly assessing mass-transport and local-environment effects. For dynamically reconstructing Cu catalysts, *ex situ* or pre-steady-state ECSA values may not accurately represent the working-state active surface. ECSA-normalized results should therefore be accompanied by geometric- and, where appropriate, mass-normalized metrics, together with a clear description of the ECSA measurement method. Device-level assessments in flow cells or MEAs should report both total C_{2+} FE and product-specific metrics (individual FE and partial current densities) together with SPCE, full-cell energy efficiency, and long-term stability, under consistently documented conditions, including CO_2 flow rate and pressure, electrolyte composition,

membrane characteristics, catalyst loading, geometric electrode area, and cell configuration. Integrated CO_2-capture and electrolysis systems additionally require clear reporting of the capture medium, release or regeneration conditions, and their effects on the electrochemical reaction environment and system-level carbon balance[187]. High FE or partial current density obtained in flow cells or MEAs should therefore not be interpreted as intrinsic catalytic activity without accounting for mass-transport and device architecture. Such reporting will help distinguish catalyst-intrinsic activity from reactor- and operating-condition-dependent effects, providing a more reliable basis for benchmarking eCO_2RR systems.

Techno-economic indicators and core engineering bottlenecks for industrial C_{2+} electrosynthesis

High FE measured in laboratory half-cells is not by itself a sufficient criterion for commercial viability. Recent techno-economic analyses of CO_2/CO electrolysis to C_{2+} products show that plant economics remain highly sensitive to electrolyzer performance, capital cost, electricity price, and downstream separation, and may face unfavorable economic margins under conventional baseline assumptions[188]. At industrially relevant current densities, full-cell energy efficiency is constrained by cathodic and anodic overpotentials, membrane and electrolyte ohmic losses, and mass-transport polarization. Techno-economic analyses of acidic-media ethylene electrosynthesis, for example, emphasize the need for low cell voltage, high selectivity, and durable membranes/catalysts to approach market competitiveness[189]. Assessments of polymer-membrane CO_2 electrolyzers further indicate that single-pass conversion and product concentration represent critical scenario-dependent targets: gaseous products may require sufficiently high single-pass conversion, whereas liquid products have been identified as requiring elevated outlet concentrations (e.g., > 3 mol L^{-1}) under evaluated techno-economic models to keep downstream separation costs manageable[190].

Carbon management and product recovery impose additional systems-level bottlenecks. In neutral and alkaline low-temperature electrolyzers, (bi)carbonate formation and crossover reduce carbon utilization, promote salt precipitation and electrode flooding, and introduce large energy penalties for CO_2 and electrolyte regeneration[191]. Process- and techno-economic analyses of carbonate-fed or bipolar-membrane-based architectures are therefore being developed to mitigate the alkaline carbon penalty and improve overall CE[192]. From a scale-up perspective, durable high-rate operation in MEA and stack configurations remains essential: long-term stability targets are typically discussed on the order of multi-thousand hours, whereas laboratory demonstrations more often report hundreds of hours under controlled conditions[193,194]. Accordingly, future progress will require concurrent advances in full-cell efficiency, SPCE, concentrated product recovery, and industrially relevant durability—not peak half-cell FE alone.

From catalyst performance to CE and lifetime in high-current devices

During ampere-level operation, gradients in local pH, K^+ and carbonate migration, salt precipitation, electrode flooding, ionomer coverage, and CO_2 crossover across the membrane can either mask or amplify intrinsic material differences[10,45,156,164]. It would therefore be preferable to compare catalysts at matched current density, gas utilization, and electrolyzer boundary conditions, within a unified framework that incorporates CE, cell voltage, energy efficiency, product separation load, and degradation rate. The demonstration of ethylene operation exceeding 150 h under strongly acidic conditions, together with the C_{2+} performance of channelized La-Cu hollow spheres approaching 1 A cm^{-2}, attests to the engineering feasibility; however, sustained long-term operation still requires addressing Cu migration, membrane fouling, salt management, and mechanical degradation[26,78,153]. Ultimately, catalyst, ionomer, membrane, pore architecture, and operating strategy would benefit from joint optimization guided by mass- and energy-balance models, rather than from isolated pursuit of peak FE.

Machine learning-assisted precise design and C_{2+} product prediction

Artificial intelligence can be embedded within the material-interface-device iterative framework described above, but it should not replace working-state validation. The first step is to establish a traceable database

that jointly records structural descriptors—including working-state Cu coordination, facet/defect ratios, valence-state lifetimes, adjacent-site distances, and *in situ* Raman/XAS signals—and operational parameters such as potential, cation identity, water activity, ionomer type, and mass-transport conditions. Prediction labels should be recorded separately for ethylene, ethanol, acetate, and C_{3+} species in terms of FE, partial current density, energy efficiency, and degradation rate, rather than collapsed into a single total C_{2+} figure[13].

As working-state atomic structures and spectroscopic time series gradually accumulate, graph neural networks can represent Cu-site adjacency and heteroatom environments, while temporal models can identify reconstruction states. Multi-task architectures may predict individual product branches such as ethylene and ethanol simultaneously, provided that FE sum rules and carbon-conservation constraints are enforced. High-accuracy molecule-Cu adsorption benchmarks, single-atom-alloy DFT calculations, and microkinetic or multiscale mass-transport models can each contribute distinct physical features spanning adsorption energies, site geometries, coupling barriers, intermediate coverages, and local pH[48,49,173]. For the time being, these algorithms are best regarded as promising but unvalidated methodological routes whose transferability needs to be tested through prospective experiments across different materials, research groups, and electrolyzer configurations.

Automated electrocatalysis platforms offer a practical entry point for active learning. Recent work has demonstrated rapid screening of rare-earth-modified Cu bimetallic systems via automated synthesis and testing[168], confirming that composition, operating conditions, and product analysis can indeed form a closed loop. However, if the platform optimizes solely for the highest total C_{2+} FE under fixed flow rates, fixed cell geometry, and short-duration steady state, the algorithm risks conflating apparatus-specific bias with intrinsic material trends. A more informative next step would be to reformulate the objective function as a multi-objective Pareto front that simultaneously constrains single-product partial current, cell voltage, CE, and degradation rate, while allowing the model to actively select replicate experiments for noise estimation. In this framing, machine learning serves to narrow the search space and quantify uncertainty, whereas mechanistic experiments and engineering evaluation remain the arbiters of whether a given structure is truly effective.

CONCLUSION

In summary, the design target for Cu-based C_{2+} electrosynthesis should shift from "the catalyst as prepared" to "the catalytic interface under operation". Crystal facets, defects, valence states, and secondary metals become meaningful only insofar as they sustain adjacent Cu sites and establish appropriate intermediate coverages; confinement, surface modification, and electrolyte engineering are productive only when they simultaneously accommodate adequate transport of CO_2, ions, and water. These structural and interfacial features can continuously evolve under applied bias; reliable structure-selectivity relationships should therefore be established using operando measurements and models that account for surface reconstruction. Moreover, promoting initial C-C bond formation must be distinguished from controlling subsequent branching toward ethylene, ethanol, acetate, or C_{3+} products.

Performance evaluation should accordingly extend beyond total C_{2+} FE. Product-specific Faradaic efficiencies and partial current densities should be reported together with SPCE, full-cell energy efficiency, product concentration, and long-term stability. H-cells, flow cells, and MEAs serve complementary purposes and should not be compared solely through their peak Faradaic efficiencies. At industrially relevant current densities, catalyst reconstruction, carbonate formation, salt precipitation, electrode flooding, and catalyst-layer degradation further require coordinated optimization of the catalyst, ionomer, membrane, pore architecture, and operating conditions. By integrating operando characterization, theory, and standardized

performance evaluation together with device-level engineering within a common workflow, empirical screening can be progressively transformed into testable design rules, moving the field closer to the selective, stable and predictable synthesis of individual multi-carbon products[26,168].

DECLARATIONS

Authors' contributions

Literature collection, critical analysis, drafting, and revision of the manuscript: Chen, Y.; Wang, Z.; Li, Y.

Availability of data and materials

Not applicable.

AI and AI-assisted tools statement

Not applicable.

Financial support and sponsorship

This work was financially supported by the Key R&D Program of Zhejiang (No. 2024C03136).

Conflicts of interest

All authors declared that there are no conflicts of interest.

Ethical approval and consent to participate

Not applicable.

Consent for publication

Not applicable.

Copyright

© The Author(s) 2026.

REFERENCES

1. Xiao, C.; Zhang, J. Architectural design for enhanced C_2 product selectivity in electrochemical CO_2 reduction using Cu-based catalysts: a review. *ACS. Nano.* **2021**, *15*, 7975-8000. DOI PubMed
2. Yan, T.; Chen, X.; Kumari, L.; et al. Multiscale CO_2 electrocatalysis to C_{2+} products: reaction mechanisms, catalyst design, and device fabrication. *Chem. Rev.* **2023**, *123*, 10530-83. DOI PubMed
3. Li, L.; Li, X.; Sun, Y.; Xie, Y. Rational design of electrocatalytic carbon dioxide reduction for a zero-carbon network. *Chem. Soc. Rev.* **2022**, *51*, 1234-52. DOI PubMed
4. Wan, C.; Fang, Y.; Li, L.; et al. Molecular bridge enables dual-intermediate synergy for selective CO_2 electroreduction to multicarbon products. *Angew. Chem. Int. Ed.* **2026**, *65*, e6511351. DOI PubMed
5. Hori, Y.; Kikuchi, K.; Suzuki, S. Production of CO and CH_4 in electrochemical reduction of CO_2 at metal electrodes in aqueous hydrogencarbonate solution. *Chem. Lett.* **1985**, *14*, 1695-8. DOI
6. Hori, Y.; Wakebe, H.; Tsukamoto, T.; Koga, O. Electrocatalytic process of CO selectivity in electrochemical reduction of CO_2 at metal electrodes in aqueous media. *Electrochim. Acta.* **1994**, *39*, 1833-9. DOI
7. Wan, C.; Qiao, P.; Zhou, Y.; et al. Programming reaction-network bifurcations for selective amino acid electrosynthesis. *J. Am. Chem. Soc.* **2026**, *148*, 32528-41. DOI PubMed
8. Kuhl, K. P.; Cave, E. R.; Abram, D. N.; Jaramillo, T. F. New insights into the electrochemical reduction of carbon dioxide on metallic copper surfaces. *Energy. Environ. Sci.* **2012**, *5*, 7050-9. DOI
9. Reske, R.; Mistry, H.; Behafarid, F.; Roldan, Cuenya. B.; Strasser, P. Particle size effects in the catalytic electroreduction of CO_2 on Cu nanoparticles. *J. Am. Chem. Soc.* **2014**, *136*, 6978-86. DOI PubMed
10. Dinh, C. T.; Burdyny, T.; Kibria, M. G.; et al. CO_2 electroreduction to ethylene via hydroxide-mediated copper catalysis at an abrupt interface. *Science* **2018**, *360*, 783-7. DOI PubMed
11. Li, L.; Wan, C.; Wang, S.; Li, X.; Sun, Y.; Xie, Y. Tandem dual-site PbCu electrocatalyst for high-rate and selective glycine synthesis at industrial current densities. *Nano. Lett.* **2024**, *24*, 2392-9. DOI PubMed

12. Schouten, K. J. P.; Kwon, Y.; van der Ham, C. J. M.; Qin, Z.; Koper, M. T. M. A new mechanism for the selectivity to C_1 and C_2 species in the electrochemical reduction of carbon dioxide on copper electrodes. *Chem. Sci.* **2011**, *2*, 1902-9. DOI
13. Chang, B.; Pang, H.; Raziq, F.; et al. Electrochemical reduction of carbon dioxide to multicarbon (C_{2+}) products: challenges and perspectives. *Energy. Environ. Sci.* **2023**, *16*, 4714-58. DOI
14. Wang, X.; Wang, Z.; García de Arquer, F. P.; et al. Efficient electrically powered CO_2-to-ethanol via suppression of deoxygenation. *Nat. Energy.* **2020**, *5*, 478-86. DOI
15. Wang, F.; Lu, Z.; Guo, H.; Hao, G.; Jiang, W.; Liu, G. Copper-based catalysts for CO_2 electroreduction to $C_{2/2+}$ products: advance and perspective. *Coord. Chem. Rev.* **2024**, *515*, 215962. DOI
16. Woldu, A. R.; Huang, Z.; Zhao, P.; Hu, L.; Astruc, D. Electrochemical CO_2 reduction (CO_2RR) to multi-carbon products over copper-based catalysts. *Coord. Chem. Rev.* **2022**, *454*, 214340. DOI
17. Liu, S.; Zhang, B.; Zhang, L.; Sun, J. Rational design strategies of Cu-based electrocatalysts for CO_2 electroreduction to C_2 products. *J. Energy. Chem.* **2022**, *71*, 63-82. DOI
18. Niu, Y.; Zhang, J.; Tang, X.; et al. Recent advances in Cu-based catalysts for electrocatalytic CO_2 reduction reaction to C_{2+} products: oxidation state of metal centers, crystal facet and micro morphology of catalyst structure. *Coord. Chem. Rev.* **2025**, *540*, 216763. DOI
19. Hussain, M. S.; Ahmed, S.; Irshad, M.; et al. Recent engineering strategies for enhancing C_{2+} product formation in copper-catalyzed CO_2 electroreduction. *Nano. Mater. Sci.* **2026**, *8*, 207-33. DOI
20. Zhan, C.; Dattila, F.; Rettenmaier, C.; et al. Key intermediates and Cu active sites for CO_2 electroreduction to ethylene and ethanol. *Nat. Energy.* **2024**, *9*, 1485-96. DOI PubMed PMC
21. Gao, W.; Xu, Y.; Fu, L.; Chang, X.; Xu, B. Experimental evidence of distinct sites for CO_2-to-CO and CO conversion on Cu in the electrochemical CO_2 reduction reaction. *Nat. Catal.* **2023**, *6*, 885-94. DOI
22. Tan, X.; Yu, C.; Ren, Y.; Cui, S.; Li, W.; Qiu, J. Recent advances in innovative strategies for the CO_2 electroreduction reaction. *Energy. Environ. Sci.* **2021**, *14*, 765-80. DOI
23. Loiudice, A.; Lobaccaro, P.; Kamali, E. A.; et al. Tailoring copper nanocrystals towards C_2 products in electrochemical CO_2 reduction. *Angew. Chem. Int. Ed.* **2016**, *55*, 5789-92. DOI PubMed
24. Zhuang, T. T.; Liang, Z. Q.; Seifitokaldani, A.; et al. Steering post-C–C coupling selectivity enables high efficiency electroreduction of carbon dioxide to multi-carbon alcohols. *Nat. Catal.* **2018**, *1*, 421-8. DOI
25. de Ruiter, J.; Benning, V. R. M.; Yang, S.; et al. Multiscale X-ray scattering elucidates activation and deactivation of oxide-derived copper electrocatalysts for CO_2 reduction. *Nat. Commun.* **2025**, *16*, 373. DOI PubMed PMC
26. Kok, J.; Albertini, P. P.; Leemans, J.; Buonsanti, R.; Burdyny, T. Overcoming copper stability challenges in CO_2 electrolysis. *Nat. Rev. Mater.* **2025**, *10*, 550-63. DOI
27. Zhao, Z. H.; Ren, D. Unravelling the effect of crystal facet of derived-copper catalysts on the electroreduction of carbon dioxide under unified mass transport condition. *Angew. Chem. Int. Ed.* **2025**, *64*, e202415590. DOI PubMed
28. Lei, Q.; Huang, L.; Yin, J.; et al. Structural evolution and strain generation of derived-Cu catalysts during CO_2 electroreduction. *Nat. Commun.* **2022**, *13*, 4857. DOI PubMed PMC
29. Ma, Y.; Yu, J.; Sun, M.; et al. Confined growth of silver–copper Janus nanostructures with {100} facets for highly selective tandem electrocatalytic carbon dioxide reduction. *Adv. Mater.* **2022**, *34*, 2110607. DOI PubMed
30. Cai, Z.; Cao, N.; Zhang, F.; et al. Hierarchical Ag-Cu interfaces promote C-C coupling in tandem CO_2 electroreduction. *Appl. Catal. B.* **2023**, *325*, 122310. DOI
31. Luo, T.; Liu, K.; Fu, J.; et al. Tandem catalysis on adjacent active motifs of copper grain boundary for efficient CO_2 electroreduction toward C_2 products. *J. Energy. Chem.* **2022**, *70*, 219-23. DOI
32. Lim, C. Y. J.; Yilmaz, M.; Arce-Ramos, J. M.; et al. Surface charge as activity descriptors for electrochemical CO_2 reduction to multi-carbon products on organic-functionalised Cu. *Nat. Commun.* **2023**, *14*, 335. DOI PubMed PMC
33. Monteiro, M. C. O.; Dattila, F.; Hagedoorn, B.; García-Muelas, R.; López, N.; Koper, M. T. M. Absence of CO_2 electroreduction on copper, gold and silver electrodes without metal cations in solution. *Nat. Catal.* **2021**, *4*, 654-62. DOI
34. Zou, H.; Cheng, D.; Tang, C.; et al. Electronic perturbation of Cu nanowire surfaces with functionalized graphdiyne for enhanced CO_2 reduction reaction. *Natl. Sci. Rev.* **2024**, *11*, nwae253. DOI PubMed PMC
35. Wu, Z.; Yang, P.; Gao, M. Dynamic evolution of copper-based catalysts during CO_2 electroreduction. *Nano. Mater. Sci.* **2026**, *8*, 687-702. DOI
36. Sakshi; Rana, S. P. S.; Abahussain, A. A. M.; Singh, L. Advances in copper-based electrocatalysts for electrochemical reduction of CO_2 to ethanol: operando, theoretical, and empirical perspectives. *Coord. Chem. Rev.* **2025**, *535*, 216672. DOI

37. Tabassum, H.; Yang, X.; Zou, R.; Wu, G. Surface engineering of Cu catalysts for electrochemical reduction of CO_2 to value-added multi-carbon products. *Chem. Catal.* **2022**, *2*, 1561-93. DOI
38. Peng, J.; Sun, L.; Li, Y.; et al. Engineering Cu-based catalysts for CO_2 electroreduction: from catalyst design to practical applications. *Electrochem. Energy. Rev.* **2025**, *8*, 16. DOI
39. Wang, X.; Hu, Q.; Li, G.; Yang, H.; He, C. Recent advances and perspectives of electrochemical CO_2 reduction toward C_{2+} products on Cu-based catalysts. *Electrochem. Energy. Rev.* **2022**, *5*, 28. DOI
40. Ye, W.; Guo, X.; Ma, T. A review on electrochemical synthesized copper-based catalysts for electrochemical reduction of CO_2 to C_{2+} products. *Chem. Eng. J.* **2021**, *414*, 128825. DOI
41. Zhang, W.; Yang, Y.; Guo, D.; Liu, L. Recent progress on copper catalysts with different surface states for CO_2 electroreduction. *J. Energy. Chem.* **2024**, *88*, 10-27. DOI
42. Vos, R. E.; Sun, P.; Schauermann, D.; et al. CO_2 electroreduction on Cu operates via an alternative chain growth mechanism to form C–C bonds at elevated temperature and pressure. *Nat. Catal.* **2025**, *8*, 1338-47. DOI PubMed PMC
43. Zhang, Z.; Li, H.; Shao, Y.; et al. Molecular understanding of the critical role of alkali metal cations in initiating CO_2 electroreduction on Cu(100) surface. *Nat. Commun.* **2024**, *15*, 612. DOI PubMed PMC
44. Deacon-Price, C.; Changeur, L.; Santana, C. S.; Garcia, A. C. The effect of the tetraalkylammonium cation in the electrochemical CO_2 reduction reaction on copper electrode. *ACS. Catal.* **2024**, *14*, 12928-39. DOI PubMed PMC
45. Zhang, H.; Gao, J.; Raciti, D.; Hall, A. S. Promoting Cu-catalysed CO_2 electroreduction to multicarbon products by tuning the activity of H_2O. *Nat. Catal.* **2023**, *6*, 807-17. DOI
46. Zhang, H.; Wang, X.; Sun, Y.; et al. Targeted C-O bond cleavage of $*CH_2CHO$ at copper active sites for efficient electrosynthesis of ethylene from CO_2 reduction. *Appl. Catal. B. Environ. Energy.* **2024**, *351*, 123992. DOI
47. Li, J.; Maresi, I.; Lum, Y.; Ager, J. W. Effects of surface diffusion in electrocatalytic CO_2 reduction on Cu revealed by kinetic Monte Carlo simulations. *J. Chem. Phys.* **2021**, *155*, 164701. DOI PubMed
48. Chen, Z.; Liu, Z.; Xu, X. Accurate descriptions of molecule-surface interactions in electrocatalytic CO_2 reduction on the copper surfaces. *Nat. Commun.* **2023**, *14*, 936. DOI PubMed PMC
49. Liu, T.; Song, G.; Liu, X.; et al. Insights into the mechanism in electrochemical CO_2 reduction over single-atom copper alloy catalysts: a DFT study. *iScience* **2023**, *26*, 107953. DOI PubMed PMC
50. Cheng, T.; Xiao, H.; Goddard, W. A. Reaction mechanisms for the electrochemical reduction of CO_2 to CO and formate on the Cu(100) surface at 298 K from quantum mechanics free energy calculations with explicit water. *J. Am. Chem. Soc.* **2016**, *138*, 13802-5. DOI PubMed
51. Yao, K.; Li, J.; Ozden, A.; et al. In situ copper faceting enables efficient CO_2/CO electrolysis. *Nat. Commun.* **2024**, *15*, 1749. DOI PubMed PMC
52. Chuai, H.; Liu, S.; Liang, Z.; Liu, H.; Zhao, Q.; Zhang, S. Identification of the C_1/C_2-forming dynamic active sites in CO_2 electroreduction on copper oxide. *Chem. Eng. J.* **2025**, *518*, 164497. DOI
53. Choi, M.; Bae, S.; Kim, Y.; et al. Selective formaldehyde condensation on phosphorus-rich copper catalyst to produce liquid C_{3+} chemicals in electrocatalytic CO_2 reduction. *Nat. Catal.* **2025**, *8*, 476-86. DOI
54. Zhang, Y.; Zhao, X.; Lang, X.; et al. Electrochemical CO_2 reduction to ethylene or ethanol via regulating Cu geometric structure. *Appl. Surf. Sci.* **2025**, *712*, 164233. DOI
55. Zou, T.; Veenstra, F. L. P.; Ibáñez-Alé, E.; et al. Chlorine-promoted copper catalysts for CO_2 electroreduction into highly reduced products. *Cell. Rep. Phys. Sci.* **2023**, *4*, 101294. DOI
56. Kurihara, R.; Nagita, K.; Ohashi, K.; et al. Carbon monoxide reduction reaction to produce multicarbon products in acidic electrolytes using gas diffusion electrode loaded with copper nanoparticles. *Adv. Mater. Interfaces.* **2023**, *11*, 2300731. DOI
57. Mustafa, A.; Lougou, B. G.; Shuai, Y.; et al. Analyzing the electrochemical reduction of CO and CO_2 as reactants to C_1 and C_2 products on copper-based flow-through gas diffusion electrodes. *J. Environ. Chem. Eng.* **2023**, *11*, 111528. DOI
58. Huang, Y.; Handoko, A. D.; Hirunsit, P.; Yeo, B. S. Electrochemical reduction of CO_2 using copper single-crystal surfaces: effects of CO* coverage on the selective formation of ethylene. *ACS. Catal.* **2017**, *7*, 1749-56. DOI
59. Yang, F.; Jiang, S.; Liu, S.; et al. Dynamics of bulk and surface oxide evolution in copper foams for electrochemical CO_2 reduction. *Commun. Chem.* **2024**, *7*, 66. DOI PubMed PMC
60. Lian, Z.; Dattila, F.; López, N. Stability and lifetime of diffusion-trapped oxygen in oxide-derived copper CO_2 reduction electrocatalysts. *Nat. Catal.* **2024**, *7*, 401-11. DOI

61. Albertini, P. P.; Newton, M. A.; Wang, M.; et al. Hybrid oxide coatings generate stable Cu catalysts for CO_2 electroreduction. *Nat. Mater.* **2024**, *23*, 680-7. DOI PubMed PMC
62. Deng, B.; Zhao, X.; Li, Y.; Huang, M.; Zhang, S.; Dong, F. Active site identification and engineering during the dynamic evolution of copper-based catalysts for electrocatalytic CO_2 reduction. *Sci. China. Chem.* **2022**, *66*, 78-95. DOI
63. Cheng, D.; Nguyen, K. L. C.; Sumaria, V.; et al. Structure sensitivity and catalyst restructuring for CO_2 electro-reduction on copper. *Nat. Commun.* **2025**, *16*, 4064. DOI PubMed PMC
64. Wei, M.; Li, J.; Zhao, J.; et al. Stabilization of oxidized Cu species via CeO_x nano-islands for enhanced CO_2 reduction to C_{2+} products. *Natl. Sci. Rev.* **2025**, *12*, nwaf351. DOI PubMed PMC
65. Wu, Z. Z.; Zhang, X. L.; Niu, Z. Z.; et al. Identification of Cu(100)/Cu(111) interfaces as superior active sites for CO dimerization during CO_2 electroreduction. *J. Am. Chem. Soc.* **2022**, *144*, 259-69. DOI PubMed
66. Li, L.; Zhou, Y.; Wan, C.; et al. Neighboring nonmetal site as an intermediate modulator switching CO_2 electroreduction pathway toward multicarbons. *Joule* **2025**, *9*, 101926. DOI
67. Wang, S.; Li, F.; Zhao, J.; et al. Manipulating C-C coupling pathway in electrochemical CO_2 reduction for selective ethylene and ethanol production over single-atom alloy catalyst. *Nat. Commun.* **2024**, *15*, 10247. DOI PubMed PMC
68. Zhang, X. Y.; Lou, Z. X.; Chen, J.; et al. Direct OC-CHO coupling towards highly C_{2+} products selective electroreduction over stable Cu^0/Cu^{2+} interface. *Nat. Commun.* **2023**, *14*, 7681. DOI PubMed PMC
69. Gao, X.; Jiang, Y.; Liu, J.; et al. Intermediate-regulated dynamic restructuring at Ag-Cu biphasic interface enables selective CO_2 electroreduction to C_{2+} fuels. *Nat. Commun.* **2024**, *15*, 10331. DOI PubMed PMC
70. Chen, C.; Yu, S.; Yang, Y.; et al. Exploration of the bio-analogous asymmetric C–C coupling mechanism in tandem CO_2 electroreduction. *Nat. Catal.* **2022**, *5*, 878-87. DOI
71. Herzog, A.; Lopez Luna, M.; Jeon, H. S.; et al. Operando Raman spectroscopy uncovers hydroxide and CO species enhance ethanol selectivity during pulsed CO_2 electroreduction. *Nat. Commun.* **2024**, *15*, 3986. DOI PubMed PMC
72. Zhang, Y.; Chen, Y.; Wang, X.; et al. Low-coordinated copper facilitates the $*CH_2CO$ affinity at enhanced rectifying interface of Cu/Cu_2O for efficient CO_2-to-multicarbon alcohols conversion. *Nat. Commun.* **2024**, *15*, 5172. DOI PubMed PMC
73. Fan, L.; Li, F.; Liu, T.; et al. Atomic-level Cu active sites enable energy-efficient CO_2 electroreduction to multicarbon products in strong acid. *Nat. Synth.* **2024**, *4*, 262-70. DOI
74. Koolen, C. D.; Pedersen, J. K.; Zijlstra, B.; et al. Scalable synthesis of Cu-cluster catalysts via spark ablation for the electrochemical conversion of CO_2 to acetaldehyde. *Nat. Synth.* **2025**, *4*, 336-46. DOI
75. Long, C.; Liu, X.; Wan, K.; et al. Regulating reconstruction of oxide-derived Cu for electrochemical CO_2 reduction toward n-propanol. *Sci. Adv.* **2023**, *9*, eadi6119. DOI PubMed PMC
76. Kim, I.; Lee, G. B.; Kim, S.; et al. Unveiling the reconstruction of copper bimetallic catalysts during CO_2 electroreduction. *Nat. Catal.* **2025**, *8*, 697-713. DOI
77. Wang, S.; Fang, Z.; Yu, C.; et al. Securing interfacial cationic copper for acidic CO_2 reduction to ethylene. *Nat. Commun.* **2025**, *16*, 10727. DOI PubMed PMC
78. Feng, J.; Wu, L.; Song, X.; et al. CO_2 electrolysis to multi-carbon products in strong acid at ampere-current levels on La-Cu spheres with channels. *Nat. Commun.* **2024**, *15*, 4821. DOI PubMed PMC
79. Qian, Z.; Han, G.; Tan, Y.; et al. σ-π dative bond stabilizing copper active site drives CO_2 electrocatalysis to hydrocarbon. *Nat. Commun.* **2025**, *16*, 11265. DOI PubMed PMC
80. Shen, Y.; Fang, N.; Liu, X.; et al. Observation of metal-organic interphase in Cu-based electrochemical CO_2-to-ethanol conversion. *Nat. Commun.* **2025**, *16*, 2073. DOI PubMed PMC
81. Yu, X.; Xu, Y.; Li, L.; et al. Coverage enhancement accelerates acidic CO_2 electrolysis at ampere-level current with high energy and carbon efficiencies. *Nat. Commun.* **2024**, *15*, 1711. DOI PubMed PMC
82. Chen, Y.; Li, X. Y.; Chen, Z.; et al. Efficient multicarbon formation in acidic CO_2 reduction via tandem electrocatalysis. *Nat. Nanotechnol.* **2023**, *19*, 311-8. DOI PubMed
83. Chen, J.; Qiu, H.; Zhao, Y.; et al. Selective and stable CO_2 electroreduction at high rates via control of local H_2O/CO_2 ratio. *Nat. Commun.* **2024**, *15*, 5893. DOI PubMed PMC
84. Zhu, C.; Wu, G.; Chen, A.; et al. Selective CO_2 electroreduction to multicarbon products exceeding 2 A cm^{-2} in strong acids via a hollow-fiber Cu penetration electrode. *Energy. Environ. Sci.* **2024**, *17*, 510-7. DOI

85. da Cunha, S. C.; Resasco, J. Maximizing single-pass conversion does not result in practical readiness for CO_2 reduction electrolyzers. *Nat. Commun.* **2023**, *14*, 5513. DOI PubMed PMC
86. Moore, T.; Oyarzun, D. I.; Li, W.; et al. Electrolyzer energy dominates separation costs in state-of-the-art CO_2 electrolyzers: implications for single-pass CO_2 utilization. *Joule* **2023**, *7*, 782-96. DOI
87. Chen, D.; Liu, J.; Yuan, Y.; et al. Electrocatalytic CO_2 reduction to ethylene in an acid-fed membrane electrode assembly at 10 A. *Nat. Commun.* **2025**, *16*, 10783. DOI PubMed PMC
88. Zhong, D.; Cheng, D.; Fang, Q.; Liu, Y.; Li, J.; Zhao, Q. Understanding the restructuring and degradation of oxide-derived copper during electrochemical CO_2 reduction. *Chem. Eng. J.* **2023**, *470*, 143907. DOI
89. Zhang, G.; Zhao, Z. J.; Cheng, D.; et al. Efficient CO_2 electroreduction on facet-selective copper films with high conversion rate. *Nat. Commun.* **2021**, *12*, 5745. DOI PubMed PMC
90. Zhang, H.; He, C.; Han, S.; et al. Crystal facet-dependent electrocatalytic performance of metallic Cu in CO_2 reduction reactions. *Chin. Chem. Lett.* **2022**, *33*, 3641-9. DOI
91. Qiao, Y.; Seger, B. Recent advances in single crystal and facet dependency of copper electrodes on electrochemical CO_2 reduction. *Curr. Opin. Chem. Eng.* **2024**, *43*, 100999. DOI
92. Xue, L.; Qi, Y.; Li, Z.; Yang, H.; Liu, R.; Zhang, B. Rational design of copper alloy electrocatalysts for electrocatalytic CO_2 reduction. *J. Energy. Chem.* **2025**, *110*, 88-108. DOI
93. Chen, P.; Wu, Y.; Rufford, T. E.; Wang, L.; Wang, G.; Wang, Z. Organic molecules involved in Cu-based electrocatalysts for selective CO_2 reduction to C_{2+} products. *Mater. Today. Chem.* **2023**, *27*, 101328. DOI
94. Castro-Castillo, C.; Nanda, K. K.; Mardones-Herrera, E.; et al. Growth direction and exposed facets of Cu/Cu_2O nanostructures affect product selectivity in CO_2 electroreduction. *Mater. Chem. Phys.* **2022**, *278*, 125650. DOI
95. Tănase, L. C.; Prieto, M. J.; de Souza Caldas, L.; et al. Morphological and chemical state effects in pulsed CO_2 electroreduction on Cu(100) unveiled by correlated spectro-microscopy. *Nat. Catal.* **2025**, *8*, 881-90. DOI
96. He, X.; Lin, L.; Li, X.; et al. Roles of copper(I) in water-promoted CO_2 electrolysis to multi-carbon compounds. *Nat. Commun.* **2024**, *15*, 9923. DOI PubMed PMC
97. Yang, Y.; Louisia, S.; Yu, S.; et al. Operando studies reveal active Cu nanograins for CO_2 electroreduction. *Nature* **2023**, *614*, 262-9. DOI PubMed
98. Amirbeigiarab, R.; Tian, J.; Herzog, A.; et al. Atomic-scale surface restructuring of copper electrodes under CO_2 electroreduction conditions. *Nat. Catal.* **2023**, *6*, 837-46. DOI
99. Cheng, D.; Zhao, Z. J.; Zhang, G.; et al. The nature of active sites for carbon dioxide electroreduction over oxide-derived copper catalysts. *Nat. Commun.* **2021**, *12*, 395. DOI PubMed PMC
100. Choi, W.; Chae, Y.; Liu, E.; et al. Exploring the influence of cell configurations on Cu catalyst reconstruction during CO_2 electroreduction. *Nat. Commun.* **2024**, *15*, 8345. DOI PubMed PMC
101. Grosse, P.; Yoon, A.; Rettenmaier, C.; Herzog, A.; Chee, S. W.; Roldan Cuenya, B. Dynamic transformation of cubic copper catalysts during CO_2 electroreduction and its impact on catalytic selectivity. *Nat. Commun.* **2021**, *12*, 6736. DOI PubMed PMC
102. Han, Z.; Han, D.; Chen, Z.; et al. Steering surface reconstruction of copper with electrolyte additives for CO_2 electroreduction. *Nat. Commun.* **2022**, *13*, 3158. DOI PubMed PMC
103. Yang, C.; Liang, S.; Zhang, C.; et al. Cu vacancies in in-situ reconstructed Cu_xSe catalysts enhancing C_{2+} production in CO_2 electroreduction. *J. Energy. Chem.* **2025**, *111*, 354-64. DOI
104. Mu, S.; Lu, H.; Wu, Q.; et al. Hydroxyl radicals dominate reoxidation of oxide-derived Cu in electrochemical CO_2 reduction. *Nat. Commun.* **2022**, *13*, 3694. DOI PubMed PMC
105. Li, G.; Liu, H.; Yang, H.; et al. Tuning product distributions of CO_2 electroreduction over copper foil through cathodic corrosion. *Chem. Eng. Sci.* **2022**, *263*, 118142. DOI
106. Yu, H.; Zhao, W.; Dong, X.; et al. Revisiting the origin of enhanced C_{2+} selectivity on oxide-derived copper toward CO_2 electroreduction. *Appl. Catal. B. Environ. Energy.* **2025**, *363*, 124805. DOI
107. Fang, Q.; Zhang, Z.; Yang, X.; Cheng, T.; Ma, X.; Tang, J. Cu_2O nanoparticles with controlled surface roughness for CO_2 electroreduction towards C_{2+} products. *Chem. Eng. J.* **2025**, *515*, 163293. DOI
108. Wang, X.; Klingan, K.; Klingenhof, M.; et al. Morphology and mechanism of highly selective Cu(II) oxide nanosheet catalysts for carbon dioxide electroreduction. *Nat. Commun.* **2021**, *12*, 794. DOI PubMed PMC
109. Ren, X.; Wang, J.; Wu, H.; et al. Cu–O geometric coordination induced facet evolution of derived Cu catalysts for efficient CO_2 electroreduction. *Sci. China. Mater.* **2025**, *68*, 3322-31. DOI

110. Wu, Q.; Chen, R.; Zhu, J.; Wang, S.; Wu, Y.; Sun, Y. In situ reconstructed interface-engineered Cu nanosheets for industrial-current-density CO_2 electroreduction to C_{2+} products. *Sci. China. Mater.* **2025**, *68*, 2358-64. DOI

111. Yang, R.; Zeng, Z.; Peng, Z.; Xie, J.; Huang, Y.; Wang, Y. Amorphous urchin-like copper@nanosilica hybrid for efficient CO_2 electroreduction to C_{2+} products. *J. Energy. Chem.* **2021**, *61*, 290-6. DOI

112. Kim, J. Y.; Hong, D.; Lee, J. C.; et al. Quasi-graphitic carbon shell-induced Cu confinement promotes electrocatalytic CO_2 reduction toward C_{2+} products. *Nat. Commun.* **2021**, *12*, 3765. DOI PubMed PMC

113. Ma, L.; Liu, H.; Mei, B.; et al. Cu supraparticles with enhanced mass transfer and abundant C-C coupling sites achieving ampere-level CO_2-to-C_{2+} electrosynthesis. *Nat. Commun.* **2025**, *16*, 3421. DOI PubMed PMC

114. Fang, Q.; Jia, Y.; Lang, X.; et al. Defect-rich porous Cu with abundant Cu(100) for acidic CO_2 electroreduction in membrane electrode assembly. *Adv. Sci.* **2025**, *12*, e10161. DOI PubMed PMC

115. Shekhawat, A.; Das, D.; Zerdoumi, R.; et al. Defect-induced selectivity modulation using copper triazole molecular frameworks for electrochemical CO_2 reduction. *Adv. Funct. Mater.* **2025**, *35*, 2506172. DOI

116. Li, B.; Xue, X.; Hong, S.; et al. 3DOM perovskite enabled interfacial microenvironment regulation with accelerated complete reconstruction to grain-boundary-rich nano-copper for high-current C_{2+} electrosynthesis. *Adv. Mater.* **2026**, *38*, e73086. DOI PubMed

117. Frisch, M. L.; Wu, L.; Atlan, C.; et al. Unraveling the synergistic effects of Cu-Ag tandem catalysts during electrochemical CO_2 reduction using nanofocused X-ray probes. *Nat. Commun.* **2023**, *14*, 7833. DOI PubMed PMC

118. Zhang, X.; Liu, C.; Zhao, Y.; et al. Atomic nickel cluster decorated defect-rich copper for enhanced C_2 product selectivity in electrocatalytic CO_2 reduction. *Appl. Catal. B.* **2021**, *291*, 120030. DOI

119. Wang, L.; Chen, Z.; Xiao, Y.; et al. Stabilized $Cu^{\delta+}$-OH species on in situ reconstructed Cu nanoparticles for CO_2-to-C_2H_4 conversion in neutral media. *Nat. Commun.* **2024**, *15*, 7477. DOI PubMed PMC

120. Zhu, J.; Wang, S.; Zhang, J.; et al. Stabilizing Cu^0/Cu^{2+} interface by hydroxy-rich amorphous SiO_2 for enhanced electrocatalytic CO_2 reduction to ethylene. *Chem. Eng. J.* **2024**, *494*, 153189. DOI

121. Liu, Y.; Liu, H.; Wang, C.; Wang, Y.; Lu, J.; Wang, H. Reconstructed Cu/Cu_2O(I) catalyst for selective electroreduction of CO_2 to C_{2+} products. *Electrochem. Commun.* **2023**, *150*, 107474. DOI

122. Yang, F.; Fang, W.; Wang, Q.; Deng, P.; Xia, B. Y. Optimizing copper oxidation state to promote ethylene generation in efficient carbon dioxide conversion. *ACS. Sustain. Chem. Eng.* **2022**, *10*, 4677-82. DOI

123. Qu, Y.; Zheng, W.; Wang, P.; et al. Creating interfaces of Cu^0/Cu^+ in oxide-derived copper catalysts for electrochemical CO_2 reduction to multi-carbon products. *J. Colloid. Interface. Sci.* **2023**, *645*, 735-42. DOI PubMed

124. Wang, M.; Fei, X.; Ning, H.; Hu, H.; Wu, M. Transient thermal shock induced radial gradient Cu^+-Ov-Ce^{3+}/Ce^{4+} boosted CO_2 electroreduction to C_2 products. *J. Energy. Chem.* **2026**, *114*, 639-45. DOI

125. Zhou, Z.; Liang, S.; Xiao, J.; et al. Surface modification of Cu_2O with stabilized Cu^+ for highly efficient and stable CO_2 electroreduction to C_{2+} chemicals. *J. Energy. Chem.* **2023**, *84*, 277-85. DOI

126. Yue, K.; Qin, Y.; Huang, H.; et al. Stabilized Cu^0 -Cu^{1+} dual sites in a cyanamide framework for selective CO_2 electroreduction to ethylene. *Nat. Commun.* **2024**, *15*, 7820. DOI PubMed PMC

127. Zhang, F.; Cao, N.; Wang, C.; et al. In situ stabilization of Cu^+ for CO_2 electroreduction via environmental-molecules-induced ZnO_{1-x} shield. *Nat. Commun.* **2025**, *16*, 6082. DOI PubMed PMC

128. Wang, S.; Wang, D.; Tian, B.; et al. Synergistic Cu^+/Cu^0 on Cu_2O-Cu interfaces for efficient and selective C_{2+} production in electrocatalytic CO_2 conversion. *Sci. China. Mater.* **2023**, *66*, 1801-9. DOI

129. Li, Y.; Shi, H.; Li, C.; et al. Shaping hollow spherical assemblies for enhanced Cu^0/Cu^+ interface to boost C_{2+} selectivity in CO_2 electroreduction. *Sci. China. Mater.* **2024**, *67*, 3596-601. DOI

130. Wu, H.; Huang, L.; Timoshenko, J.; et al. Selective and energy-efficient electrosynthesis of ethylene from CO_2 by tuning the valence of Cu catalysts through aryl diazonium functionalization. *Nat. Energy.* **2024**, *9*, 422-33. DOI

131. Liu, L.; Lv, Y.; Yue, M.; et al. Enhancing CO_2 electroreduction to multi-carbon products via Ca-stabilized Cu^0/Cu^+ heterointerface. *Appl. Catal. B. Environ. Energy.* **2026**, *388*, 126550. DOI

132. Lv, X.; Liu, Q.; Wang, J.; et al. Grain refining enables mixed Cu^+/Cu^0 states for CO_2 electroreduction to C_{2+} products at high current density. *Appl. Catal. B.* **2023**, *324*, 122272. DOI

133. Chen, H.; Wang, Z.; Wei, X.; et al. Promotion of electrochemical CO_2 reduction to ethylene on phosphorus-doped copper nanocrystals with stable $Cu^{\delta+}$ sites. *Appl. Surf. Sci.* **2021**, *544*, 148965. DOI

134. Chen, W.; Li, M.; Cheng, Y.; et al. Eu-doped Cu_2O for tailored Cu^+/Cu^0 sites and enhanced C_2 selectivity in CO_2 electroreduction. *Appl. Surf. Sci.* **2025**, *690*, 162633. DOI

135. Vavra, J.; Ramona, G. P. L.; Dattila, F.; et al. Solution-based Cu^+ transient species mediate the reconstruction of copper electrocatalysts for CO_2 reduction. *Nat. Catal.* **2024**, *7*, 89-97. DOI

136. Cui, P.; Zou, Y.; Wang, J.; et al. In situ construction of Co-lattice OD-Cu/Cu_2O heterostructure for highly active CO_2-to-ethylene conversion via strong additive-metal oxide interaction. *Adv. Funct. Mater.* **2026**, *36*, e76245. DOI

137. Yang, C.; Wang, R.; Yu, C.; et al. Engineering stable Cu^+-Cu^0 sites and oxygen defects in boron-doped copper oxide for electrocatalytic reduction of CO_2 to C_{2+} products. *Chem. Eng. J.* **2024**, *484*, 149710. DOI

138. Cao, X.; Ren, S.; Zhang, X.; et al. Identification of $Cu^0/Cu^+/Cu^0$ interface as superior active sites for CO_2 electroreduction to C_{2+} in neutral condition. *Chem* **2024**, *10*, 2089-102. DOI

139. Zhang, L. L.; Wang, K. A.; Zhu, G. R.; Shi, J. Y.; Zhu, H. B. Assembly of colloidal Cu nanoparticles and Ni-N-C nanocarbons to electrochemically boost cascade production of ethylene from CO_2 reduction. *J. Mater. Sci.* **2023**, *58*, 17200-10. DOI

140. Li, X.; Wang, J.; Lv, X.; et al. Hetero-interfaces on Cu electrode for enhanced electrochemical conversion of CO_2 to multi-carbon products. *Nano. Micro. Lett.* **2022**, *14*, 134. DOI PubMed PMC

141. Chhetri, M.; Wan, M.; Jin, Z.; et al. Dual-site catalysts featuring platinum-group-metal atoms on copper shapes boost hydrocarbon formations in electrocatalytic CO_2 reduction. *Nat. Commun.* **2023**, *14*, 3075. DOI PubMed PMC

142. Möller, T.; Filippi, M.; Brückner, S.; Ju, W.; Strasser, P. A CO_2 electrolyzer tandem cell system for CO_2-CO co-feed valorization in a Ni-N-C/Cu-catalyzed reaction cascade. *Nat. Commun.* **2023**, *14*, 5680. DOI PubMed PMC

143. Zhao, Q.; Wang, J.; Zhuang, Y.; et al. In situ reconstruction of Bi nanoparticles confined within 3D nanoporous Cu to boost CO_2 electroreduction. *Sci. China. Mater.* **2024**, *67*, 796-803. DOI

144. Yang, Y.; Fu, H.; Xiao, C.; Du, X.; Song, Z. Efficient electrochemical CO_2 reduction to C_{2+} hydrocarbons on Zn-doped Cu films. *Appl. Surf. Sci.* **2024**, *646*, 158866. DOI

145. Chen, J.; Chowdhury, M. H.; Ghosh, S.; et al. Palladium-enhanced copper nitride anti-perovskite nanocrystals boosting CO_2 electroreduction to C_2 products. *Chem. Eng. J.* **2025**, *522*, 168044. DOI

146. Shan, J.; Shi, Y.; Li, H.; et al. Effective CO_2 electroreduction toward C_2H_4 boosted by Ce-doped Cu nanoparticles. *Chem. Eng. J.* **2022**, *433*, 133769. DOI

147. da Silva, A. H. M.; Raaijman, S. J.; Santana, C. S.; Assaf, J. M.; Gomes, J. F.; Koper, M. T. M. Reprint of "electrocatalytic CO_2 reduction to C_{2+} products on Cu and Cu_xZn_y electrodes: effects of chemical composition and surface morphology". *J. Electroanal. Chem.* **2021**, *896*, 115609. DOI

148. Luo, Y.; Yang, J.; Qin, J.; et al. Cobalt phthalocyanine promoted copper catalysts toward enhanced electro reduction of CO_2 to C_2: synergistic catalysis or tandem catalysis? *J. Energy. Chem.* **2024**, *92*, 499-507. DOI

149. Zhang, J.; Pham, T. H. M.; Ko, Y.; et al. Tandem effect of Ag@C@Cu catalysts enhances ethanol selectivity for electrochemical CO_2 reduction in flow reactors. *Cell. Rep. Phys. Sci.* **2022**, *3*, 100949. DOI

150. Plaza-Mayoral, E.; Okatenko, V.; Dalby, K. N.; et al. Composition effects of electrodeposited Cu-Ag nanostructured electrocatalysts for CO_2 reduction. *iScience* **2024**, *27*, 109933. DOI PubMed PMC

151. Deng, H.; Liu, T.; Zhao, W.; et al. Substituent tuning of Cu coordination polymers enables carbon-efficient CO_2 electroreduction to multi-carbon products. *Nat. Commun.* **2024**, *15*, 9706. DOI PubMed PMC

152. Ding, M.; Tang, L.; Ma, X.; Song, C.; Wang, S. Effects of ligand tuning and core doping of atomically precise copper nanoclusters on CO_2 electroreduction selectivity. *Commun. Chem.* **2022**, *5*, 172. DOI PubMed PMC

153. Chen, Q.; Tan, Y.; Wang, X.; et al. Long-term stable acidic electroreduction of CO_2 to C_2 products at industrial current density using passivated copper. *Nat. Commun.* **2025**, *16*, 8468. DOI PubMed PMC

154. Xie, W.; Tian, T.; Yue, S.; et al. Synergistic surface modification of Cu with Schiff-base networks for high selectivity and durability in CO_2-to-C_2H_4 electroreduction. *Nat. Commun.* **2026**, *17*, 3968. DOI PubMed PMC

155. Zeng, F.; Wang, X.; Yin, T.; et al. Polymer-tethered pyridine tunes activities of the two distinct CO_2 electroreduction sites on Cu. *Nat. Commun.* **2025**, *16*, 11511. DOI PubMed PMC

156. El-Nagar, G. A.; Haun, F.; Gupta, S.; Stojkovikj, S.; Mayer, M. T. Unintended cation crossover influences CO_2 reduction selectivity in Cu-based zero-gap electrolysers. *Nat. Commun.* **2023**, *14*, 2062. DOI PubMed PMC

157. Zhang, Z. M.; Wang, T.; Cai, Y. C.; et al. Probing electrolyte effects on cation-enhanced CO_2 reduction on copper in acidic media. *Nat. Catal.* **2024**, *7*, 807-17. DOI

158. Zhang, J.; Huang, J.; Zhang, S.; et al. Confinement-driven CO spillover in CuAg@MSN tandem catalysts boosts C_2 selectivity toward electrocatalytic CO_2 reduction. *Adv. Sci.* **2026**, *13*, e76068. DOI PubMed PMC

159. Bi, J.; Li, P.; Liu, J.; et al. Construction of 3D copper-chitosan-gas diffusion layer electrode for highly efficient CO_2 electrolysis to C_{2+} alcohols. *Nat. Commun.* **2023**, *14*, 2823. DOI PubMed PMC

160. Liu, Y. Y.; Zhu, H. L.; Liao, P. Q.; Chen, X. M. A stable copper-based metal-azolate framework for efficient electroreduction of CO_2 to C_{2+} products. *Chem. Res. Chin. Univ.* **2024**, *40*, 664-9. DOI

161. Tan, Z.; Zhang, J.; Yang, Y.; et al. Polymeric ionic liquid promotes acidic electrocatalytic CO_2 conversion to multicarbon products with ampere level current on Cu. *Nat. Commun.* **2025**, *16*, 1843. DOI PubMed PMC

162. Chen, X.; Zhu, C.; Liu, Q.; et al. Simultaneous coating of benzotriazole and polyvinyl chloride on Cu for improved CO_2 electroreduction toward C_2 products. *Chem. Eng. J.* **2026**, *529*, 173047. DOI

163. Zhao, T.; Zong, X.; Liu, J.; et al. Functionalizing Cu nanoparticles with fluoric polymer to enhance C_{2+} product selectivity in membraned CO_2 reduction. *Appl. Catal. B.* **2024**, *340*, 123281. DOI

164. Kim, C.; Bui, J. C.; Luo, X.; et al. Tailored catalyst microenvironments for CO_2 electroreduction to multicarbon products on copper using bilayer ionomer coatings. *Nat. Energy.* **2021**, *6*, 1026-34. DOI

165. Yu, J.; Zheng, Y.; Lv, B.; et al. Structural transformation of copper-coordinated COFs drives enhanced multi-carbon selectivity in CO_2 electroreduction. *Appl. Catal. B. Environ. Energy.* **2025**, *368*, 125131. DOI

166. Li, X. Q.; Duan, G. Y.; Chen, J. W.; Han, L. J.; Zhang, S. J.; Xu, B. H. Regulating electrochemical CO_2RR selectivity at industrial current densities by structuring copper@poly(ionic liquid) interface. *Appl. Catal. B.* **2021**, *297*, 120471. DOI

167. Zhang, H.; Zhu, C.; Liu, R.; Fang, Q.; Song, S.; Shen, Y. Insight into the island-sea effect of Cu-N−C for enhanced CO_2 eletroreduction selectively towards C_2H_4. *Appl. Catal. B.* **2024**, *343*, 123566. DOI

168. Shen, Y.; Wang, Z.; Wang, Y.; Wang, C. Rapid screening of copper-based bimetallic catalysts via automatic electrocatalysis platform: electrocatalytic reduction of CO_2 to C_{2+} products on europium-modified copper. *Artif. Intell. Chem.* **2024**, *2*, 100056. DOI

169. Huš, M.; Likozar, B. Reengineering the old wingmen: increasing K^+ coverage to boost electrocatalytic CO_2RR on Cu. *Chem. Catal.* **2023**, *3*, 100611. DOI

170. Lin, S.; Fishler, Y.; Kwon, S.; et al. Cooperative effects associated with high electrolyte concentrations in driving the conversion of CO_2 to C_2H_4 on copper. *Chem. Catal.* **2025**, *5*, 101338. DOI

171. Lu, X.; Gankhuyag, T.; Obata, K.; Yu, Y.; Takanabe, K. Selectivity control by modifying pressure, temperature, and ionomer decoration for CO_2 electroreduction using gas-diffusion Cu electrodes. *Chem. Catal.* **2024**, *4*, 101030. DOI

172. Rashid, M.; Nabil, S. K.; Adnan, M. A.; Kannimuthu, K.; Kibria, M. G. Cation-infused bilayer ionomer coating enables high partial current density toward multi carbon products in CO_2 electrolysis. *Adv. Energy. Mater.* **2024**, *14*, 2400570. DOI

173. Adesina, P.; Elliott, J. A.; Lapkin, A. A. Multiscale modelling of species transport in hydrophilic Nafion®-coated Cu catalysts for CO_2 electro-reduction. *Chem. Eng. J.* **2023**, *478*, 147461. DOI

174. Girichandran, N.; Saedy, S.; Kortlever, R. Electrochemical CO_2 reduction on a copper foam electrode at elevated pressures. *Chem. Eng. J.* **2024**, *487*, 150478. DOI

175. Hasa, B.; Zhao, Y.; Jiao, F. In situ/operando characterization techniques of electrochemical CO_2 reduction. *Annu. Rev. Chem. Biomol. Eng.* **2023**, *14*, 165-85. DOI PubMed

176. Yang, H.; Hu, Y. W.; Chen, J. J.; et al. Intermediates adsorption engineering of CO_2 electroreduction reaction in highly selective heterostructure Cu-based electrocatalysts for CO production. *Adv. Energy. Mater.* **2019**, *9*, 1901396. DOI

177. Yang, Y.; Shi, C.; Feijóo, J.; et al. Dynamic evolution of copper nanowires during CO_2 reduction probed by operando electrochemical 4D-STEM and X-ray spectroscopy. *J. Am. Chem. Soc.* **2024**, *146*, 23398-405. DOI PubMed

178. Yao, Y.; Shi, T.; Chen, W.; et al. A surface strategy boosting the ethylene selectivity for CO_2 reduction and in situ mechanistic insights. *Nat. Commun.* **2024**, *15*, 1257. DOI PubMed PMC

179. Lee, S. H.; Avilés Acosta, J. E.; Lee, D.; et al. Structural transformation and degradation of Cu oxide nanocatalysts during electrochemical CO_2 reduction. *J. Am. Chem. Soc.* **2025**, *147*, 6536-48. DOI PubMed PMC

180. Liu, Q.; Jiang, Q.; Li, L.; Yang, W. Spontaneous reconstruction of copper active sites during the alkaline CORR: degradation and recovery of the performance. *J. Am. Chem. Soc.* **2024**, *146*, 4242-51. DOI PubMed

181. Wu, H.; Yu, H.; Chow, Y. L.; Webley, P. A.; Zhang, J. Toward durable CO_2 electroreduction with Cu-based catalysts via understanding their deactivation modes. *Adv. Mater.* **2024**, *36*, 2403217. DOI PubMed

182. Nie, X.; Griffin, G. L.; Janik, M. J.; Asthagiri, A. Surface phases of $Cu_2O(111)$ under CO_2 electrochemical reduction conditions. *Catal. Commun.* **2014**, *52*, 88-91. DOI

183. Yang, Y.; Jiang, M.; Xiao, S.; et al. Quantifying the driving force for the surface reconstruction of copper under electrochemical reduction of CO_2 by first-principles simulations. *Langmuir* **2025**, *41*, 14019-26. DOI PubMed

184. Tang, Q.; Zhang, S.; Zhu, B.; Gao, Y. In situ reconstruction of a Cu(100) surface for promoted C-C coupling in CO_2 electroreduction from first-principles multiscale modeling. *ACS. Catal.* **2026**, *16*, 1325-37. DOI

185. Wei, S.; Luo, Y.; Zhang, H.; et al. Voltage-dependent electrochemical carbon dioxide reduction mechanism unveiled by kinetic Monte Carlo simulation. *J. Phys. Chem. Lett.* **2025**, *16*, 2896-904. DOI PubMed

186. Zhang, S.; Tang, Q.; Zhu, B.; Gao, Y. Reaction-driven varieties of active sites on Cu(100) in electrochemical CO_2 reduction reaction. *ACS. Catal.* **2025**, *15*, 6497-506. DOI

187. Zhang, Z.; Li, Y.; Zhong, Y.; et al. sp^2/sp^3-hybridized nitrogen-mediated electrochemical CO_2 capture and utilization. *Sci. Adv.* **2025**, *11*, eadw6592. DOI PubMed PMC

188. Sajeev, A.; Kroes, M.; Bagemihl, I.; Kortlever, R.; de Jong, W.; Ramdin, M. Process modeling and techno-economic analysis of an integrated large-scale CO_2/CO electroreduction plant to produce C_{2+} products. *Ind. Eng. Chem. Res.* **2026**, *65*, 1716-33. DOI

189. Ozden, A.; Huang, M.; Aldhanhani, S. Carbon dioxide electrolysis to ethylene - a techno-economic assessment for acidic-media systems. *Energy. Convers. Manage.* **2026**, *348*, 120710. DOI

190. Deng, W.; Lee, A.; Dai, W.; et al. Techno-economics of polymer-membrane-based CO_2 electrolysers. *Nat. Rev. Clean. Technol.* **2025**, *1*, 255-68. DOI

191. Ramdin, M.; Moultos, O. A.; van den Broeke, L. J. P.; Gonugunta, P.; Taheri, P.; Vlugt, T. J. H. Carbonation in low-temperature CO_2 electrolyzers: causes, consequences, and solutions. *Ind. Eng. Chem. Res.* **2023**, *62*, 6843-64. DOI

192. Venkataraman, A.; Song, H.; Brandão, V. D.; et al. Process and techno-economic analyses of ethylene production by electrochemical reduction of aqueous alkaline carbonates. *Nat. Chem. Eng.* **2024**, *1*, 710-23. DOI

193. Tavella, F.; Torre, M. F.; Rabino, F.; et al. Electrochemical CO_2 reduction at scale: current status, technological readiness and industrial perspective. *Chem. Eng. J.* **2026**, *537*, 176357. DOI

194. Lee, H.; Kwon, S.; Park, N.; et al. Scalable low-temperature CO_2 electrolysis: current status and outlook. *JACS. Au.* **2024**, *4*, 3383-99. DOI PubMed PMC

Disclaimer/Publisher's Note: All statements, opinions, and data contained in this publication are solely those of the individual author(s) and contributor(s) and do not necessarily reflect those of OAE and/or the editor(s). OAE and/or the editor(s) disclaim any responsibility for harm to persons or property resulting from the use of any ideas, methods, instructions, or products mentioned in the content.

© The Author(s) 2026. Open Access This article is licensed under a Creative Commons Attribution 4.0 International License (https://creativecommons.org/licenses/by/4.0/), which permits unrestricted use, sharing, adaptation, distribution and reproduction in any medium or format, for any purpose, even commercially, as long as you give appropriate credit to the original author(s) and the source, provide a link to the Creative Commons license, and indicate if changes were made.